Chapter 6: Temperature and Pressure-Induced Phase Transition and Magnetoelastic Coupling in the Hexagonal NiMnGa

This chapter contains an investigation of order of phase transitions, evidence for the magnetoelastic coupling, anomalous thermal expansion, and pressure-induced phase transition in the hexagonal NiMnGa compound using magnetization, temperature as well as pressure dependent high-resolution synchrotron x-ray powder diffraction data analysis.

6.1 Introduction

Apart from Ni-Mn-based MSMAs with cubic austenite phase, there are another class of MSMAs with hexagonal austenite phase [197]. They are termed as Mn-based *MnM′X* compounds [198, 361], where *M′* is a transition metal element while *X* is a group IIIA or IVA element. These materials have received considerable attention in recent years as they exhibit several interesting physical phenomena, magnetic shape memory effect [197], such as magnetocaloric effect [199-201], negative thermal expansion behavior [200, 210], magnetostructural coupling [196] and magnetoresistance [202], with tremendous potential for a wide ranging technological applications which includes magnetic refrigeration [199-201], multifunctional sensors/actuators [196, 197], and novel memory devices [196, 197, 202]. At high temperatures, all these compounds crystallize in the Ni_2In-type hexagonal structure with $P6_3/mmc$ space group [198, 361]. On lowering the temperatures, the high temperature hexagonal phase in one group of compounds, like MnNiGe [196, 199, 200, 362], MnCoGe [204, 208, 363], MnNiSi [205, 364], and MnCoSi [365-367], undergoes a martensitic phase transition to a TiNiSi-type orthorhombic structure in the space group *Pnma* [14] with widely varying transition temperatures T_M ~ 470 K [196], 430 K [204], 1200 K [205], and 1162 K [367]/1192 K [366], respectively. We termed these materials as group-I compounds. On the other hand, there is another group of such compounds, like MnNiGa [187, 214, 368], MnPdGa [188, 369, 370], MnPtGa [209, 234, 371], MnFeGe [372, 373] and MnCoSn [374, 375], in which the high-temperature hexagonal phase is fully stabilized without undergoing any structural/martensite transition on cooling. We termed these materials as group-II compounds. Since unit cell volume of the high temperature hexagonal phase is lower than that of the low-temperature orthorhombic phase in group-I compounds, it is reported to be stabilized by substitutions with smaller size elements [196, 200] or creation of sufficient concentration of vacancies [206, 207] or application of external hydrostatic pressure [208, 376] even in the group-I compounds. First-principles calculations seem to suggest that the stabilization of the hexagonal phase by substitution with atoms, like Fe at the Ni site in MnNiGe [196], occurs due to enhanced hybridization of the 3d orbitals of the neighboring Mn atoms [196]. Besides the hybridization factor, the role of the valence electron to atom ratio (*e/a*) in the stabilization of the hexagonal phase has also been highlighted even when there is substitution with larger size atoms, like In at the Ge-site in MnCoGe [208].

In addition to the martensite transition, both the group of compounds display interesting magnetic transitions leading to a rich variety of collinear and noncollinear magnetic structures [187, 196, 200, 204, 209, 367-369]. For example, the martensite phase of MnNiGe [196] and MnCoSi [367] undergoes a paramagnetic to a spiral antiferromagnetic (AFM) transition with T_N ~ 352 K and 400 K, whereas the martensite phase of MnCoGe [204, 377] and MnNiSi [205, 364] exhibit paramagnetic to collinear ferromagnetic (FM) phase transition with T_C ~ 345 K and 662 K, respectively. The FM T_C in the stabilized hexagonal austenite phase of the group-II compounds NiMnGa [187, 214, 368], MnPdGa [188, 369, 370], and PtMnGa [209, 234, 371] is ~350 K, 308 K, and 230 K, respectively. In group-II compounds, the FM phase undergoes a spin reorientation transition (SRT) [187, 188, 209, 214, 234, 368-371] with transition temperature T_{SRT} lying in the range 200 K [214] to 80 K [372]. Since the SRT leads to noncollinear magnetic structures [214, 368, 369, 371] with uniaxial anisotropy and extreme sensitivity to dc field (*H*) bias [370, 371], these compounds have attracted considerable attention in recent years as skyrmion host materials [214]. The discovery of an exotic biskyrmionic [185] state in a group-II compound, NiMnGa [187, 213], induced by a relatively low magnetic field (0.25 Tesla) at room temperature [187], which remains stable on the removal of the magnetic field after field cooling [378] up to the ferromagnetic $T_C \sim$ 350K, has opened new vistas for designing novel non-volatile memory devices [185, 187, 213, 378, 379]. The structure and magnetic properties of NiMnGa can be easily altered by compositional tuning [214, 380] for e.g., the hexagonal austenite phase has been experimentally achieved with substitution of larger Ga on the place of smaller Ge in MnNiGe via reduction in unit cell volume [199].

The observation of skyrmions [209] and biskyrmions [187] in these compounds necessarily implies the existence of noncollinear magnetic structures [214, 369-371] with uniaxial anisotropy [214] and strong coupling of the spin and lattice degrees of freedom [371, 381]. The study of such magnetoelastic coupling has evinced considerable focus in group-I compounds like MnNiGe [196, 200, 381] and MnCoGe [363] by shifting the martensitic transition temperature T_M below the magnetic transition temperature T_C through chemical substitutions by Fe [196, 200] and Cu [382] to induce magnetostructural transitions like in magnetic shape memory alloys (MSMAs) [100, 102]. These compositionally engineered alloys exhibit very interesting meta thermal properties like negative thermal expansion as well as nearly zero thermal expansion coefficient over a range of temperatures around the two magnetic transitions [200, 210] due to magnetovolume effect [200, 261, 262], wherein the bulk strain scales quadratically with magnetization, reminiscent of the Invar systems [200, 383], and compensates for the usual thermal expansion behavior caused by the anharmonic lattice vibrations [200, 210, 363]. In the present chapter, we show the Invar effect [200] (i.e., nearly zero thermal expansion) and anomalous thermal expansion behavior observed even in the NiMnGa (group-II compound) in which the hexagonal phase is fully stabilized without any magnetostructural transition. Previous synchrotron x-ray and neutron diffraction study on NiMnGa revealed an anomaly in the c/a ratio at T ~ 250 K linked with the collinear FM [214] to a noncollinear FM structure transition at T_{SRT} ~ 200 K [214]. Such an anomaly above a magnetic transition, in the absence of any structural or magnetostructural phase transition, is an indication of the presence of magnetoelastic effect [216, 371, 384] or isostructural phase transition [216, 217, 384]. Also, the magnetoelastic coupling with negative magnetostriction has been observed in a related sister compound (PtMnGa) using the SXRPD data [371]. This calls for a comprehensive study of magnetoelastic coupling and its consequences around both the high temperature paramagnetic to FM and the low-temperature spin reorientation transitions.

The magnetoelastic effect has been reported in skyrmions hosting B20 chiral magnets through Landau-Ginzburg free energy functional formulation [220, 224, 225]. The stability of spin textures of skyrmion are very sensitive to external uniaxial stress or pressure, which can manipulate the stability of these spin textures through intrinsic spin-lattice coupling [221-223]. Therefore, manipulation of skyrmions with the external parameter like the pressure is of great importance to improve their practical applicability [226-228]. Although the stability of skyrmions by pressure-tuning has been investigated in the noncentrosymmetric materials for e.g., MnSi [227], FeGe [228], Cu_2OSeO_3 [226, 385], there is almost negligible report in the centrosymmetric materials like biskyrmion host NiMnGa. This calls for a detailed study on the pressure-tuning of biskyrmions in the centrosymmetric NiMnGa.

Isostructural phase transition induced by pressure is an interesting phenomenon wherein the anomaly in structural parameters like lattice parameter, *c/a* ratio, or volume collapse appears without any crystallographic symmetry change [216, 385-388]. Such phase transitions always received significant attention as they are very seldom. In general, the isostructural phase transition is associated with the change in electronic structure, which reveals anomalies in the frequency of associated phonon mode [387, 388]. The electronic structure can be easily modified with pressure, which may lead to significant changes in isostructural phase transitions [387, 388]. Although there are few reports wherein the effect of hydrostatic pressure has been investigated to see the hexagonal phase stability in *MnM′X* compounds by pressure dependent magnetization measurements [208, 211, 389], a direct study of the crystal structure with pressure has not been reported yet.

In NiMnGa, the maximum density of biskyrmions has been reported at T_{SRT} ~ 200 K [187], where antiferromagnetic (AFM) components increase significantly due to spin canting [214]. The application of hydrostatic pressure at room temperature can compress the lattice and results into the reduced Mn-Mn interatomic distances, which may lead to the modification of magnetic interactions in NiMnGa as observed in skyrmion host Cu_2OSeO_3 [385]. In addition, increasing behavior of FM T_C with hydrostatic pressure (increasing rate of dT_C/dP ~ 1.7 K/kbar) [231] has been reported for a similar hexagonal sister compound PtMnGa which hosts skyrmions with maximum stability at its T_{SRT} ~ 215 K [209]. Therefore, a natural question arises: Can SRT be induced at room temperature driven by external pressure via modification in the magnetic interaction in NiMnGa? The answer will be helpful to stabilize the maximum density of biskyrmions at room temperature in NiMnGa and lead to low power consumption in the spintronic devices [214]. Further, the skyrmion host Cu_2OSeO_3 revealed dramatic enhancement in the temperature window of stable skyrmions driven by external pressure and also shows interesting pressure-driven phase transition. Therefore, a detailed pressure study of NiMnGa is required to explore the stability of biskyrmions and crystal structure under external hydrostatic pressure.

This chapter provides detailed magnetization study and crystal structure investigation using high-resolution SXRPD data of hexagonal NiMnGa. We show that low field magnetization does not follow order parameter behavior below T_C but instead exhibits an anomalous decrease below T_C, suggesting the gradual emergence of MCA eventually leading to the reported noncollinear FM structure [214] below T_{SRT}. Our magnetization data show a small thermal hysteresis across FM $T_{C,}$ indicating its first-order character, which is confirmed by the Arrott plot study based on the Banerjee criterion [284-287]. The temperature dependence of the structural parameters reveals anomalies around T_C as well as T_{SRT} and indicates the precursor effect of SRT. More significantly, the detailed analysis of bond length suggests that the Ni-Mn and Ni-Ga mediated exchange interactions play a major role in the paramagnetic to the FM phase transition. In contrast, the Mn-Mn mediated exchange interactions dominate the SRT. Evidence for the magnetoelastic coupling in the FM phase as well as SRT phase is discussed. We believe that our results on magnetoelastic coupling may provide insight towards understanding the extreme sensitivity of the magnetic textures of skyrmion to external stresses as observed in the B20 magnets [220-225]. In addition, we also present the evidence for the pressure-induced isostructural phase transition in the hexagonal NiMnGa compound using *in situ* high-pressure SXRPD data analysis up to 14 GPa, which reveals the continuous reduction of lattice parameters with nonlinearity above 4 GPa. The different compression rates of the *a*-axis in the basal plane and the *c*-axis in the prismatic plane indicate the anisotropic compression behavior. The present SXRPD study under pressure contributes to the understanding of crystal structure with the application of hydrostatic pressure in the biskyrmion host NiMnGa.

6.2 Experimental Section

The polycrystalline ingot of NiMnGa was prepared by the standard arc-melting [266] method using the appropriate quantity of each constituent with minimum of 99.99% purity. The ingot was melted several (3 to 4) times to achieve uniform composition. The as melted ingot was annealed in evacuated quartz ampoule filled with argon gas (first evacuated up to ~10^{-6} mbar and then argon filled) at 800ºC for 6 days to get further homogeneity and finally quenched in the ice-water mixture [390]. A part of the annealed ingot was crushed into powder, which was used for x-ray powder diffraction (XRD) measurements. The XRD data were recorded on an in-house high-resolution 18 kW Cu-rotating anode-based x-ray powder diffractometer fitted with a curved crystal monochromator (Rigaku). To check the chemical composition, energy dispersive analysis of x-rays (EDAX) characterization was performed using EVO-Scanning Electron Microscope MA15/18 (ZEISS) equipped with an energy dispersive spectroscopy detector (Model No. 51N1000-EDS System) in the backscattered electron mode. The average composition was found to be $Ni_{0.95}Mn_{1.05}Ga$, which corresponds to NiMnGa. The temperature dependent magnetization data were collected using vibrating sample magnetometer attachment in a physical properties measurement system (PPMS, Quantum Design). The magnetization data in the temperature range 2 to 395 K were collected during the warming cycle on zero-field cooled (ZFCW) as well as field cooled (FCW) samples. In addition, the data were also collected during the field cooling (FC) cycle in the same temperature range. The magnetic field-dependent magnetization data was also collected at selected temperatures by varying the magnetic field from -8 to 8 Tesla using the same PPMS system.

The high-resolution and high flux SXRPD patterns were recorded in the temperature range of 110 to 400 K in the 5 K interval using a wavelength of λ ~ 0.207 Å at the P02.1 beamline of PETRA-III, DESY, Germany [246]. The borosilicate capillaries were used as sample containers for the data collection. The *in situ* high-pressure SXRPD measurements were carried out using x-rays with the wavelength of 0.49584 Å at Xpress beamline at ELETTRA, Trieste, Italy [247]. The data was collected up to 14 GPa using membrane-driven diamond anvil cell (DAC) for generating the pressure. The methanol-ethanol mixture in 4:1 ratio was employed for the pressure transmitting medium. The pressure was monitored by the ruby fluorescence method wherein a few tiny ruby chips (~5–10 μm) were included along with the powder sample in the DAC pressure chamber. The diffraction data was detected using PILATUS3S-6M detector. The 2D image was integrated into 1D (intensity vs 2θ) diffraction data using FIT2D software.

6.3 Results and Discussion

6.3.1 Phase Purity

The Rietveld refinement using the laboratory XRD data is shown in Figure 6.1. The refinement was carried out using FULLPROF package [299] in the $P6_3/mmc$ space group (No. 194) considering all the atoms at special Wyckoff positions, i.e., Mn at 2a (0, 0, 0), Ni at 2d (1/3, 2/3, 3/4) and Ga at 2c (1/3, 2/3, 1/4), respectively [187, 214]. Figure 6.1 shows an excellent fit between observed and calculated profiles. This confirms the hexagonal crystal structure in the $P6_3/mmc$ space group at room temperature of NiMnGa, i.e., phase purity of the powder sample. The refined lattice parameters were found to be $a = b = 4.1574(1)$ Å and $c = 5.3261(1)$ Å. The present XRD pattern and refined lattice parameters are in good agreement with the previous report [187, 214]. The unit cell of NiMnGa is shown in the inset of Figure 6.1.

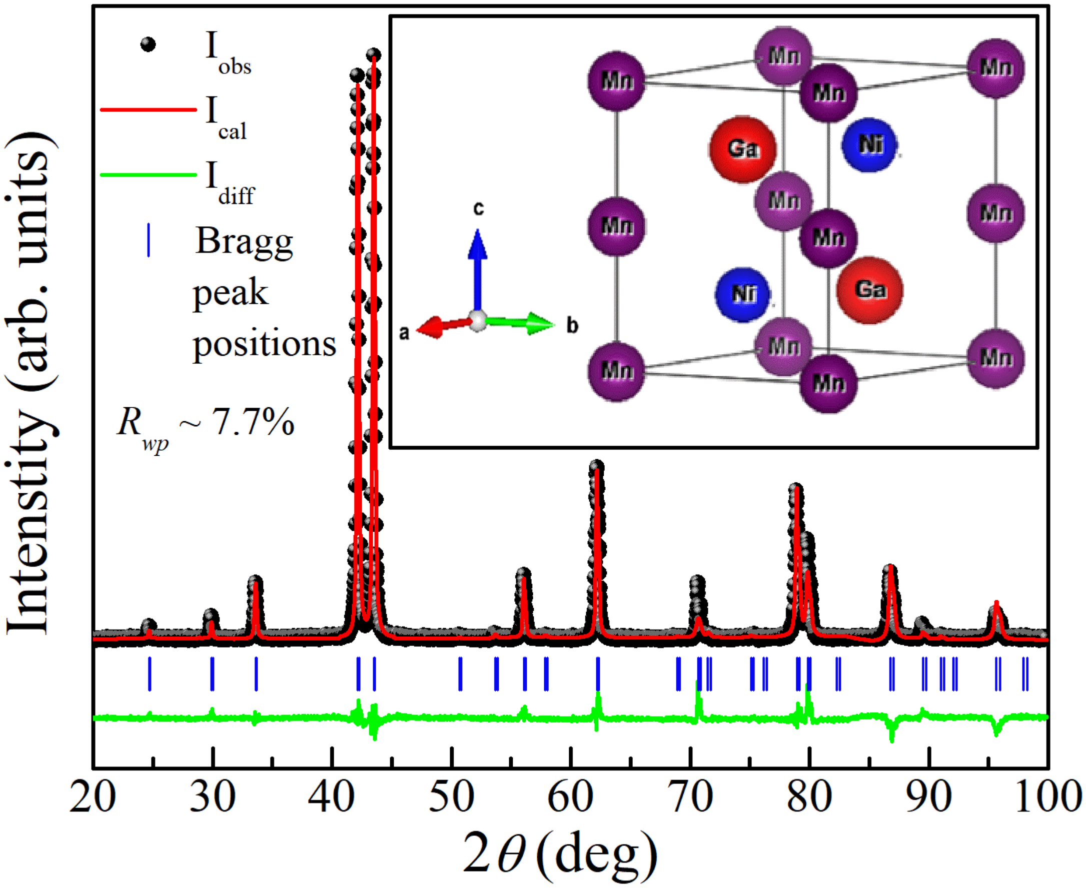

Figure 6.1: The observed (filled black circles), calculated (continuous red line), and difference (bottom green line) profiles obtained after Rietveld refinement using laboratory x-ray powder diffraction data at room temperature using the hexagonal structure with $P6_3/mmc$ space group. The vertical ticks above the difference profile represent the Bragg peak positions. The "R_{wp}" is the weighted agreement factor of the fitting. The inset depicts a unit cell structure of NiMnGa.

6.3.2 Ferromagnetic to Paramagnetic Phase Transition Behavior

The temperature dependence of magnetization (*M(T)*), measured at 100 Oe field under the ZFCW protocol, is shown in Figure 6.2. The sharp rise in magnetization around 350 K has been attributed to a phase transition from the paramagnetic state to a collinear FM phase by neutron scattering studies under zero-field bias [214]. The transition temperature T_C ~ 350 K is close to the onset of the rising part of magnetization for the warming cycle and is in good agreement with that reported in the literature [187]. Further, the mid-point of rising part of magnetization for the warming cycle is observed at T_{mid} ~ 342 K. However, the gradually decreasing behavior of the magnetization after attaining a peak value around 300 K is unlike the canonical ferromagnetic order parameter behavior as per the phenomenological theories [265], which predict that magnetization (M) should increase as per order parameter behavior $M \sim (T - T_C)^{1/2}$ after its sharp rise around the T_C. This decreasing trend of the magnetization indicates a precursor effect linked to the emergence of uniaxial magnetocrystalline anisotropy of the noncollinear canted FM structure, observed in neutron scattering studies [214], below the spin reorientation transition (SRT) temperature T_{SRT}. The SRT is marked by the appearance of a kink at ~210 K in the $M(T)$ curve for 100 Oe field, as shown more clearly in the inset (i) of Figure 6.2 using a magnified scale. Using the temperature derivative of the $M(T)$ curve at 100 Oe, the SRT temperature found at the T_{SRT} ~ 200 K corresponds to the mid-point of the SRT region shown in the inset (i) of Figure 6.2. The SRT is discussed in more detail in section 6.3.3, while the precursor effect of SRT is discussed in detail in section 6.3.4 based on temperature dependent structural parameters. Below the ~ 210 K, the magnetization falls off more rapidly. Both the precursor effect above the T_{SRT} and the rapid fall in the magnetization below the T_{SRT} disappear at high fields, as can be seen from inset (ii) of Figure 6.2, which depicts $M(T)$ collected under the ZFCW cycle at a magnetic field of 5 Tesla. This suggests that the noncollinear FM structure is unstable under sufficiently high magnetic fields in agreement with the literature [380]. The rapid decrease in $M(T)$ below 50 K in Figure 6.2 is a matter of future investigation.

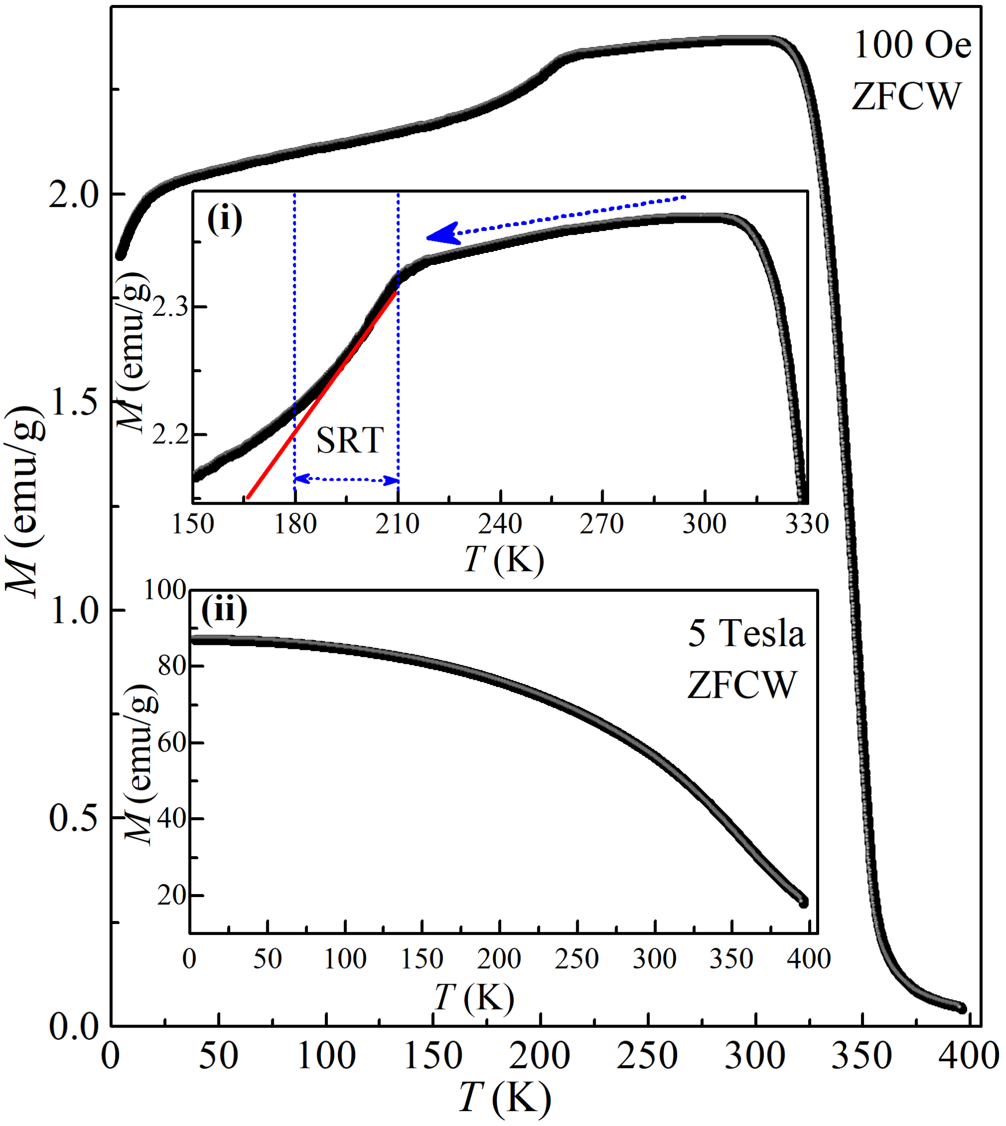

Figure 6.2: The magnetization vs temperature (*M(T)*) plot for an applied field of 100 Oe under zero-field cooled warming (ZFCW) cycle. Inset (i) depicts the enlarged view of *M(T)* in the temperature range of 150 K to 330 K where the arrow shows the decreasing behavior of *M(T)* below ferromagnetic transition temperature (T_C), the red line shows deviation below 180 K and dotted blue lines are showing the spin reorientation transition (SRT) region with starting at ~ 210 K. Inset (ii) depicts the *M(T)* measured at a high applied field (5 Tesla) under the ZFCW cycle.

Since the appearance of the skyrmionic textures below T_C is intimately linked to the noncollinear FM structure with MCA under an external magnetic field in the NiMnGa [187], it is of interest to investigate the magnetic field dependence of the both magnetic transition temperatures. Figure 6.3(a) depicts the *M(T)* measured at different magnetic fields (100 Oe, 500 Oe, 1000 Oe, 1500 Oe, 2000 Oe, and 5000 Oe) for the ZFCW, FC, and FCW cycles. The bifurcation appears between ZFCW and FC cycles at low temperatures. In principle, any thermodynamic phase transition does not exhibit bifurcation between ZFCW and FC, but the bifurcation that appeared in the present cases is due to the noncollinear FM structure that occurred below T_{SRT}. The disappearance of bifurcation at the higher field (5000 Oe) suggests the weak nature of the SRT (Figure 6.3(a)). It is interesting to note that the ZFCW and FCW *M(T)* curves nearly coincide, as expected for a thermodynamic phase transition. However, thermal hysteresis exists between the FC and FCW curves, as shown more clearly in Figure 6.3(b), which depicts the *M(T)* plot on a magnified scale. Such a thermal hysteresis points towards the first-order character of the paramagnetic to FM transition at T_C. This thermal hysteresis around T_C persists even at high fields suggesting the robustness of the first-order character of paramagnetic to FM phase transition. In fact, the temperature range of this hysteresis increases with increasing field. Although the thermal hysteresis is quite prominent, the transition itself is rather smeared out, and the diffuseness of the transition increases with the increasing magnetic field. The determination of the onset temperature (T_{onset}) of FM transition using the ZFCW curve is illustrated in Figure 6.4 for the 100 to 5000 Oe field. The inset of Figure 6.4 shows the variation of the T_{onset} as a function of the magnetic field. The linearly increasing trend of T_{onset} with the field is expected for a normal paramagnetic to FM phase transition since the field tends to stabilize the FM phase at higher temperatures.

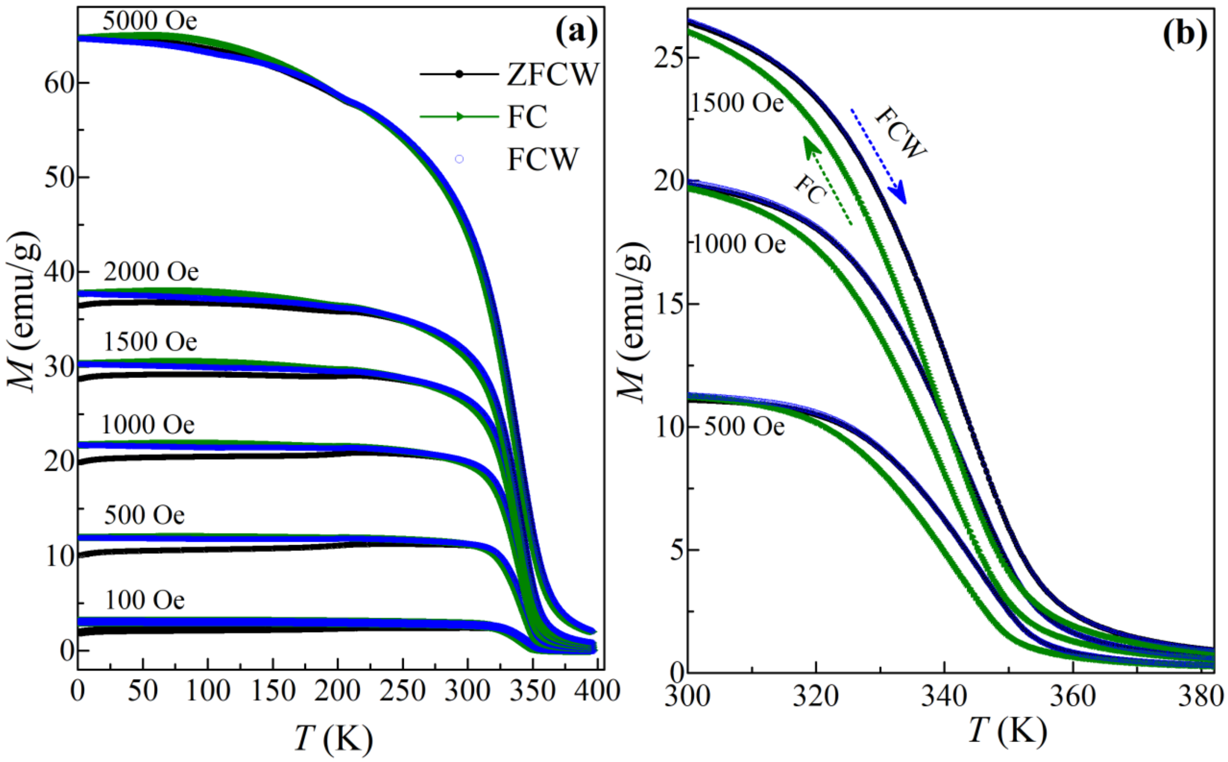

Figure 6.3: (a) *M(T)* at different magnetic applied fields under ZFCW, FC, and FCW cycles indicated by black, olive, and blue color, respectively. (b) An enlarged view of (a) around T_C at the indicated field, where ZFCW and FCW cycles are completely superimposed, while the arrow indicates the FC and FCW cycles. The ZFCW, FC, and FCW correspond to measurements performed during warming on the zero-field cooled sample, during field cooling, and during warming on the field cooled sample, respectively.

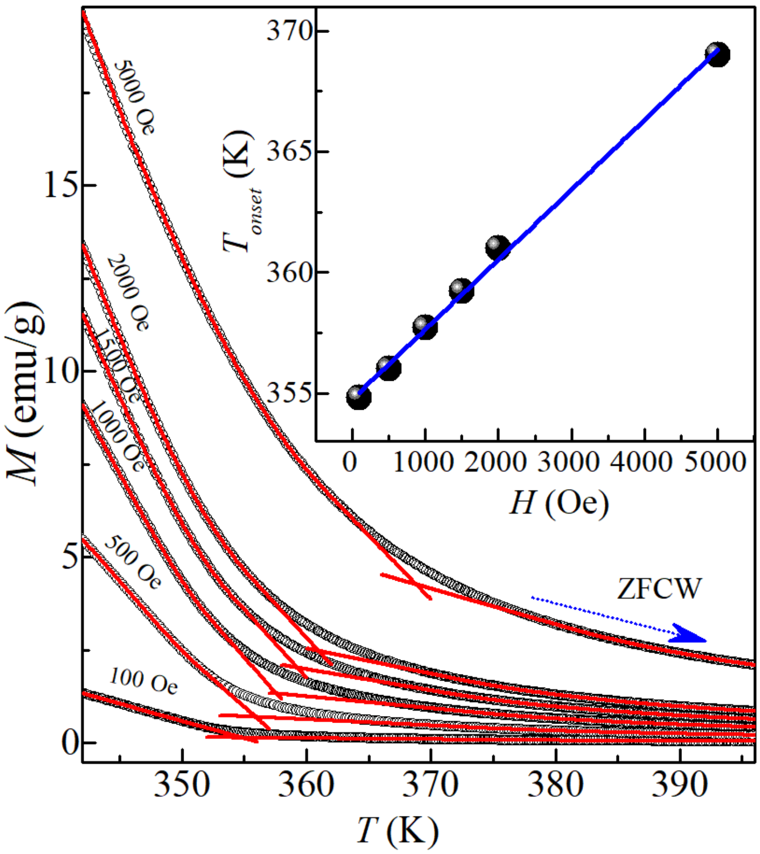

Figure 6.4: The enlarged view of Figure 6.3(a) around T_C only for the ZFCW cycle (indicated by arrow) at the indicated fields. The red lines indicate the extrapolation of magnetization for both above and below T_C where the intersection point of red lines is considered as the onset temperature of T_C (T_{onset}) at each field. The obtained T_{onset} at each field is shown in the inset, where the blue line represents the linear fitting.

The first-order nature of the paramagnetic to FM phase transition was further confirmed using Arrott plots, which have been widely used [285-287, 391-393] to obtain information about the order of the phase transition based on the Banerjee criterion [284, 285]. The field-dependent isotherms (M vs H plots), measured while cooling the sample from the paramagnetic to the FM state, in the temperature range 378 to 330 K at 2 K interval, are shown in Figure 6.5(a).

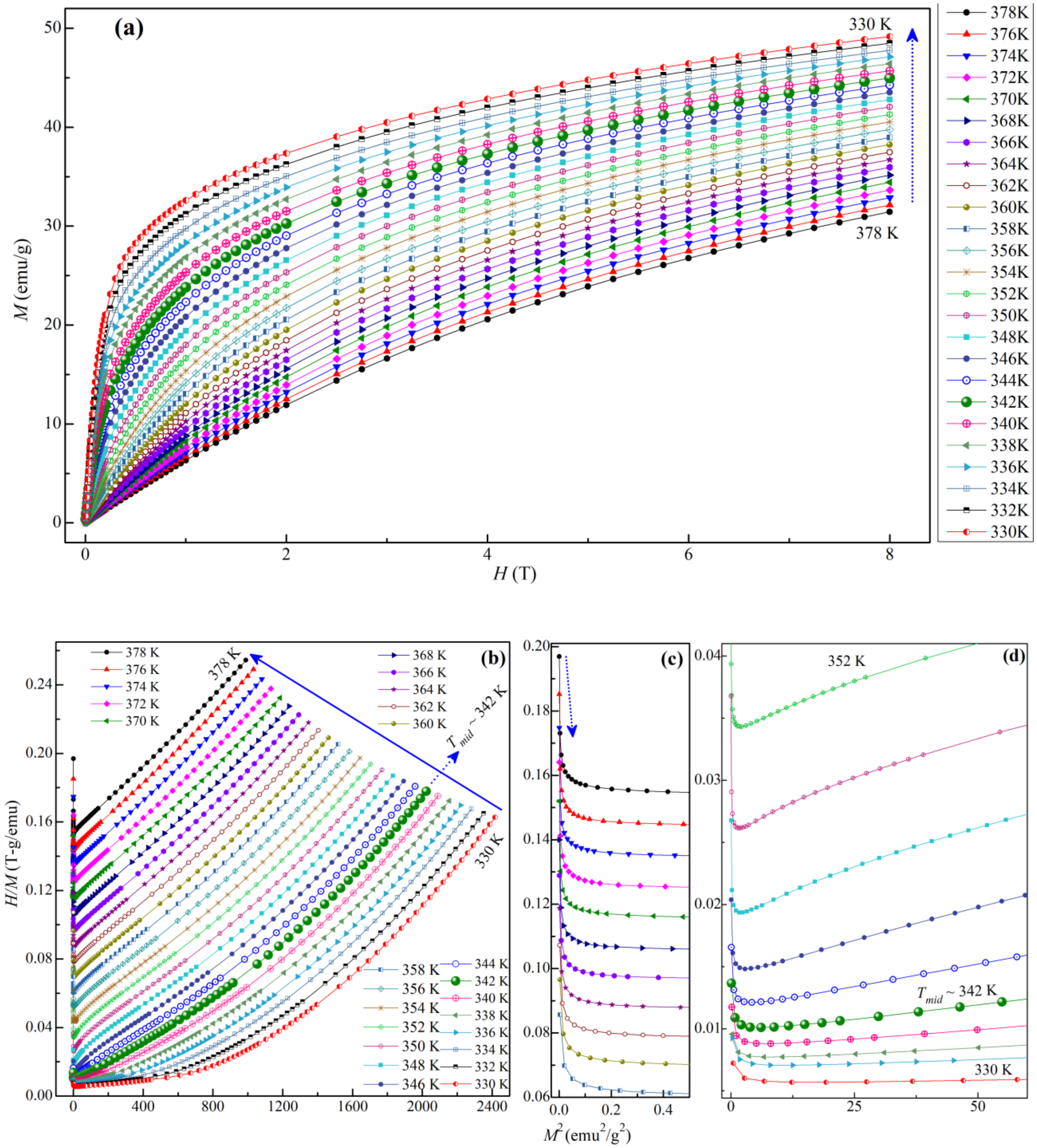

Figure 6.5: (a) The isotherms ($M(H)$) around T_C in the temperature range of 378-330 K, in the 2 K temperature interval, under the cooling cycle. (b) The Arrott plots (H/M vs M^2 plots) using $M(H)$. Figs. (c) and (d) depict enlarged views of the Arrott plots at the low field region at the indicated temperatures. The arrow in (c) is to guide the negative slope. The change of sign of curvature around T_{mid} ~ 342 K is visible in (d).

The Arrott plots (H/M vs H^2) obtained using the $M(H)$ isotherms (Figure 6.5(a)) across FM transition are shown in Figure 6.5(b), wherein T_{mid} indicate the mid-point temperature of FM transition (see discussion of section 6.3.2). Figure 6.5(c) and Figure 6.5(d) depict the enlarged view of the Arrott plots at the low field region and across T_{mid} ~ 342 K, respectively. The appearance of negative slope in the low field region and curvature change around T_{mid} ~ 342 K provide further confirmation of the first-order character of paramagnetic to FM phase transition in accordance with the Banerjee criterion [284, 285].

6.3.3 Spin Reorientation Transition Behavior

The enlarged view of $M(T)$ (shown in Figure 6.3(a)) around spin reorientation transition (SRT) for ZFCW and FC cycles at the indicated magnetic fields are shown in Figure 6.6(a) and Figure 6.6(b), respectively. The $M(T)$ at 100 Oe, 500 Oe, 1000 Oe, and 1500 Oe are stacked together to see the close view of SRT, while $M(T)$ at 2000 Oe and 5000 Oe are given separately as magnetization exhibit larger signal at such high field (please see Figure 6.6(a) & (b)). Figure 6.6(a) shows the interesting behavior of SRT. A slope change is observed at lower field values (100 Oe and 500 Oe) while a peak-like behavior at higher field values (1000 Oe and 1500 Oe). On further increasing the field up to 2000 Oe, the diffuse peak-like behavior appeared, which almost disappeared at a much higher field (5000 Oe). This suggests that the SRT is stable only at low field and become weaker at higher fields. The behavior of SRT at lower magnetic fields (100 Oe, 500Oe, 1000 Oe, and 1500 Oe) is not matching for the ZFCW and FC cycles, as evident by Figure 6.6(a) & (b). For e.g., the SRT does not appear clearly (or very weak) in the FC cycle at 100 Oe, as shown in Figure 6.6(b). The different behavior of SRT in ZFCW and FC cycles suggests the measurement history dependence behavior of SRT. The enlarged view of $M(T)$ (shown in Figure 6.3(a)) around SRT for FC and FCW cycles at 2000 Oe is shown in Figure 6.6(c), which reveals clear thermal hysteresis around T_{SRT}. The field dependency of start of the SRT temperature (T_{SRT}^{s}), which considered as the intersection point of linear fits performed above and below of the start of decreasing region in ZFCW magnetization around SRT (see Figure 6.6(a)), is shown in Figure 6.6(d). It is evident from Figure 6.6(d) that the T_{SRT}^{s} is increasing with increasing field.

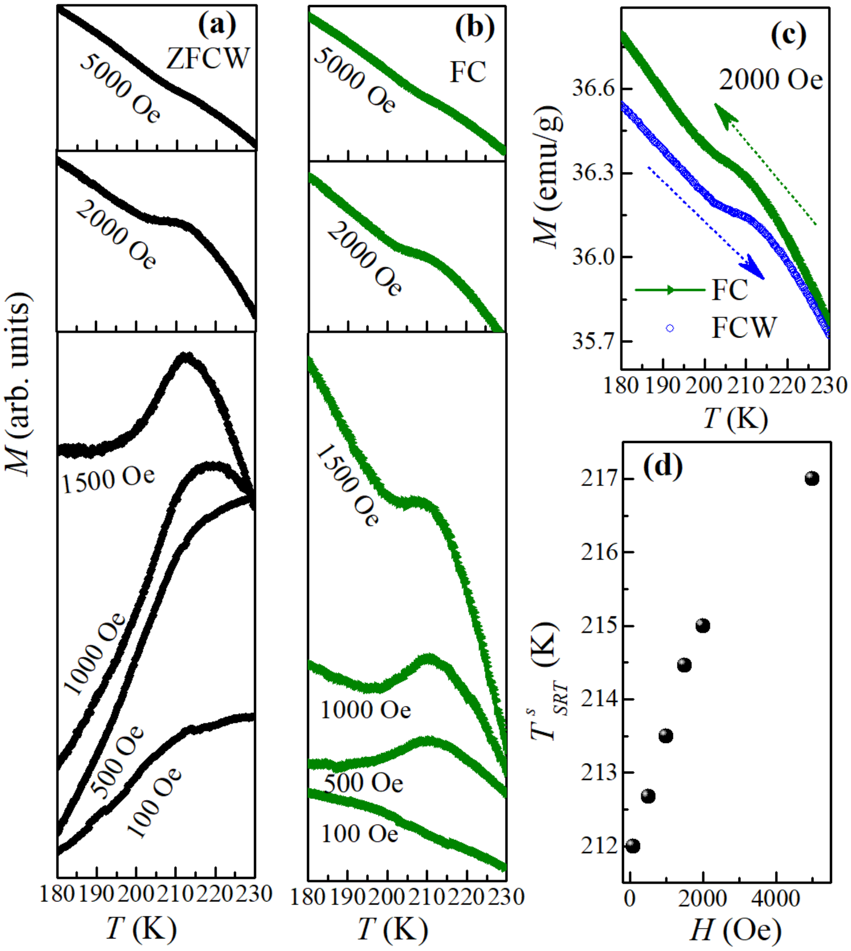

Figure 6.6:The enlarged view of *M(T)* (given in Figure 6.3(a)) at indicated fields around spin reorientation transition (SRT) for (a) ZFCW cycle and (b) FC cycle. The (c) depicts an enlarged view of *M(T)* around SRT for FC and FCW cycles guided by the arrow at 2000 Oe of the applied field. The (d) depicts the field dependence of start of the SRT temperature (T_{SRT}^{s}) (obtained from ZFCW curve).

The present increasing behavior of T^{s}_{SRT} with the field for NiMnGa is in marked contrast with the field dependency of FM-AFM-like transition in Fe-doped MnNiGe [200] alloy, where decreasing behavior of FM-AFM like transition with the field reported [200]. This is probably due to the absence of martensite transition in the hexagonal NiMnGa.

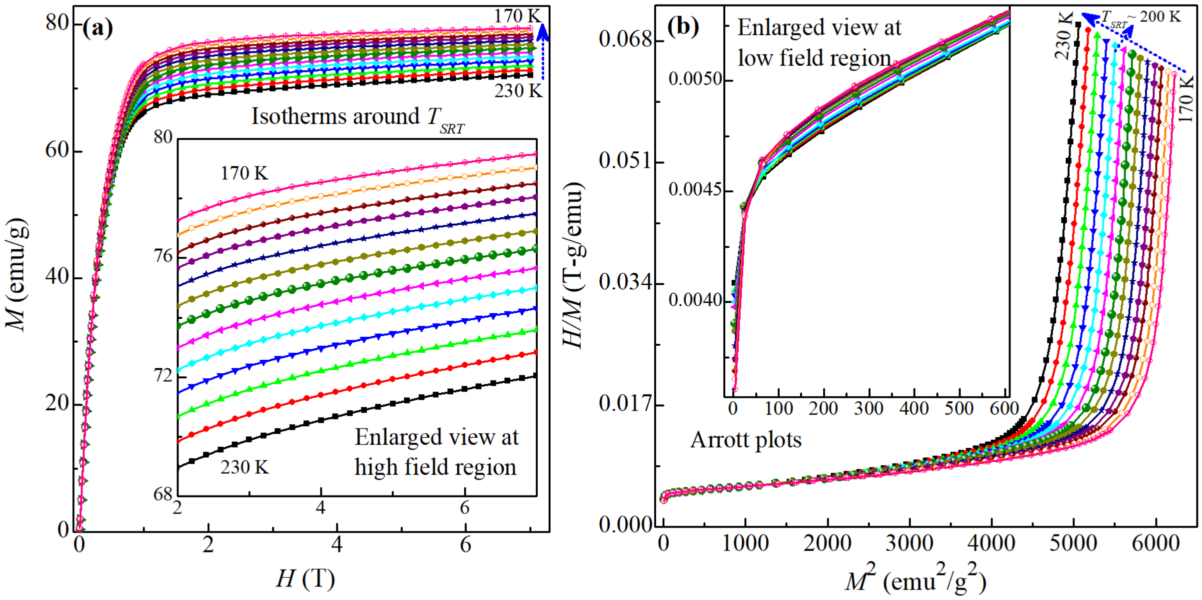

Figure 6.7: (a) Isothermal *M(H)* around T_{SRT} in the 170-230 K temperature range in the 5 K temperature interval. (b) Arrott plots using *M(H)* around T_{SRT}. The inset in (a) and (b) depict an enlarged view at the region of the high field of *M(H)* and at the low field region of the Arrott plots.

The presence of thermal hysteresis around T_{SRT} (Figure 6.6(c)), similar to the T_C motivated us to investigate the Arrott plots around T_{SRT}. In order to do that, *M(H)* data were collected around T_{SRT} ~ 200 K in the temperature range of 170-230 K in the temperature interval of 5 K (Figure 6.7(a)). The Arrott plots were obtained using this *M(H)* data are shown in Figure 6.7(b). The inset of Figure 6.7(b) shows an enlarged view at the low field region. There is the absence of any traces of negative slope in the Arrott plots around $T_{SRT,}$ as evident by the inset of Figure 6.7(b), which is probably because the theory of the Arrott plot is for paramagnetic to FM phase transition and not for inter-magnetic transitions (like FM to SRT in the present case).

6.3.4 Temperature Dependent Structure Investigation

Now, to get a better understanding of the interesting features observed in the low field (100 Oe) magnetization data (Figure 6.2), a detailed structural investigation is performed using high-resolution SXRPD data, which was collected in the temperature range of 110 K to 400 K to cover all the important features (transitions) observed in low field magnetization (Figure 6.2). The result of the Rietveld refinement using SXRPD at 300 K is shown in Figure 6.8(a), which reveals an excellent match between observed and calculated profiles for $P6_3/mmc$ space group with the hexagonal structure. The inset of Figure 6.8(a) shows an enlarged view of fit around the most intense Bragg peaks region. The refined lattice parameters (LP) at 300 K are $a = b = 4.15538(5)$ Å and $c = 5.3245(1)$ Å, which is in close agreement with those obtained from the laboratory XRD data analysis (discussed earlier in section 6.3.1). After confirming the hexagonal phase at room temperature, the SXRPD patterns at a few selected temperatures, which cover all the magnetic transitions visible in low field magnetization (Figure 6.2), are shown in Figure 6.8(b). The inset of Figure 6.8(b) depicts an enlarged view around the most intense Bragg peaks region. Further, an enlarged view of SXRPD data around the most intense Bragg peaks region in the 110-400 K range in the small temperature interval of 5 K is shown in Figure 6.8(c). It is evident from Figure 6.8(b) and (c) that there is no splitting of Bragg peaks, as well as no new peak appears with a change in the temperature suggesting the absence of any phase transition. This suggests that the hexagonal symmetry of NiMnGa remains unchanged in the temperature range of 110-400 K. In addition, the absence of phase transition below 110 K was verified using laboratory source XRD measurement at low temperature. The XRD patterns at the indicated temperature (300 to 15 K) is depicted in Figure 6.9(a) and (b), which suggests the absence of any new peak or Bain distortion down to 15 K, the minimum temperature up to which XRD was collected.

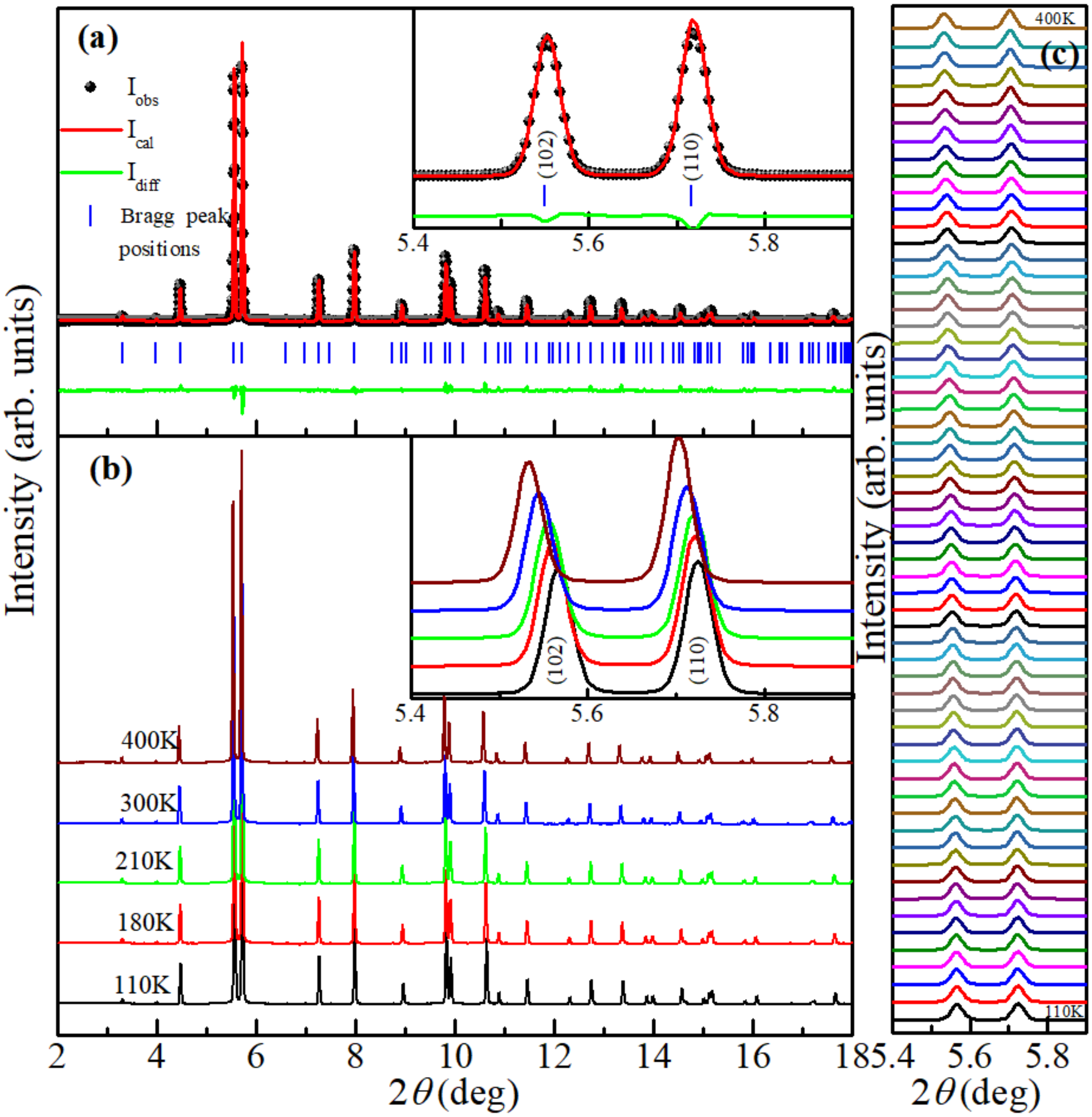

Figure 6.8: (a) The observed (filled black dots), calculated (continuous red line), and difference (bottom green line) profiles obtained after Rietveld refinement using synchrotron x-ray powder diffraction (SXRPD) data at room temperature using the hexagonal structure with $P6_3/mmc$ space group. The vertical blue ticks above the difference profile represent the Bragg peak positions. The inset of (a) depicts an enlarged view of the most intense Bragg peak region. (b) The SXRPD

patterns at the indicated temperatures. The inset of (b) depicts the enlarged view of the most intense Bragg peak region. (c) The enlarged view of SXRPD data around intense Bragg peak region in the 110-400 K range in the temperature interval of 5 K.

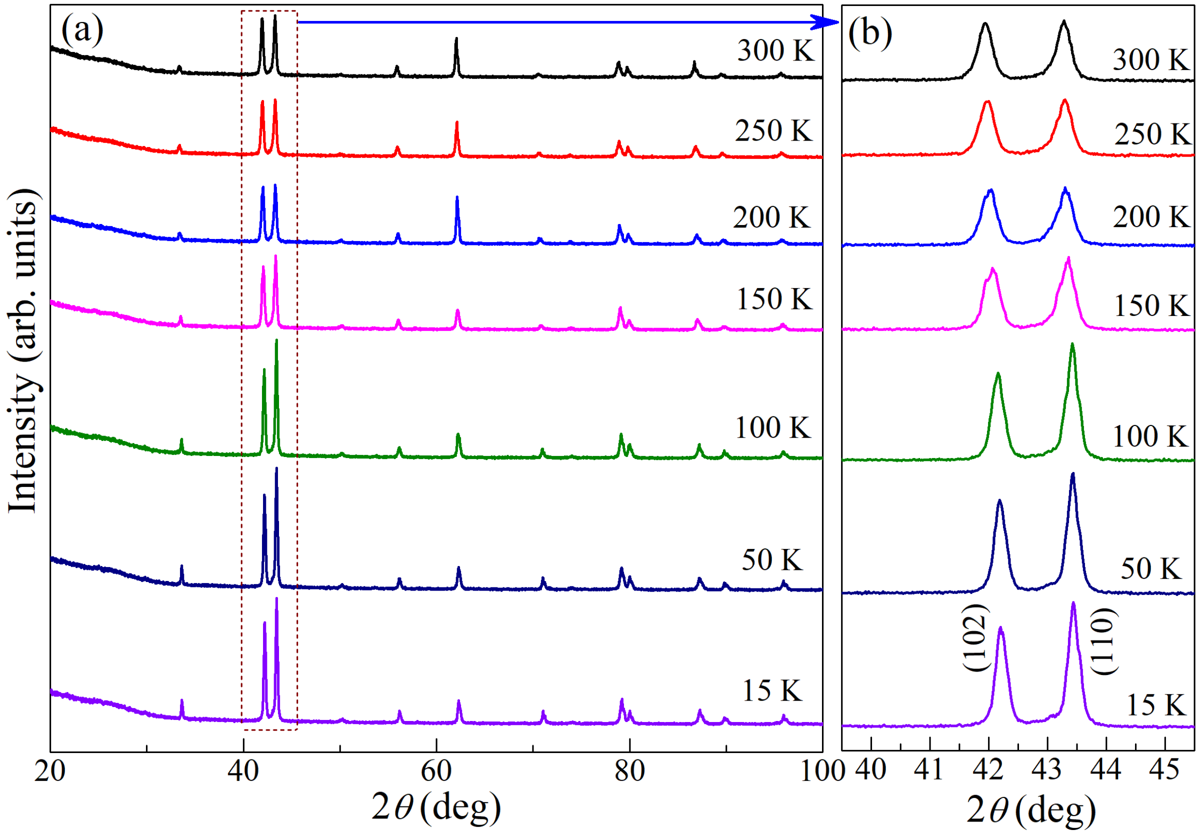

Figure 6.9: (a) The temperature dependent (300 to 15 K) laboratory source x-ray diffraction patterns of MnNiGa. (b) An enlarged view of (a) around the most intense Bragg peak region. The miller indices of both major peaks are indicated near the bottom-most pattern in (b).

The Rietveld refinement of temperature dependent SXRPD patterns was performed to get a detailed picture of the crystal structure with change in temperature in 5 K temperature interval. The parameters obtained after the Rietveld refinements at the selected temperature (400 K, 300 K, and 110 K), covering both magnetic transitions (T_C ~ 350 K and T_{SRT} ~ 200 K), are given in Table 6.1.

Table 6.1: The lattice parameters (*a* and *c*), thermal factor (B), and agreement factors obtained after Rietveld refinement (with $P6_3/mmc$ space group) using temperature dependent SXRPD data of NiMnGa.

Temperature → **Parameters ↓**	**400 K**	**300 K**	**110 K**
a (Å)	4.1627(1)	4.15538(5)	4.14626(6)
c (Å)	5.3379(2)	5.3245(1)	5.2986(1)
B_{Ni} (Å^2)	1.21(1)	1.02(3)	0.77(2)
B_{Mn} (Å^2)	0.98(5)	0.82(2)	0.40(2)
B_{Ga} (Å^2)	0.78(3)	0.61(3)	0.28(1)
χ^2	4.58	1.1	1.36
R_p	23.6	9.23	12.3
R_{wp}	30.4	13.0	16.5
R_{exp}	14.21	15.25	14.14

The temperature dependency of LP (*a* and *c*), *c/a*, unit cell volume (*V*), obtained from the Rietveld refinements, and their derivative are shown in Figure 6.10(a)-(f), where the temperatures T_C and T_{SRT} are guided by the vertical dash line. The temperature dependent LP (*a* and *c*) and *V*, shown in Figure 6.10(a) and (c), respectively, reveal a linear behavior with tiny slope change around temperatures T_C ~ 350 K and T_{SRT} ~ 200 K. The *c/a* ratio (i.e., hexagonal distortion), shown in Figure 6.10(b), exhibits much more pronounced change ~350 K and ~200 K in comparison to change in LP. To get more insight into the magnetic transitions, the temperature derivative of *a*-parameter and *c*-parameter are shown in Figure 6.10(d) and Figure 6.10(e), respectively, where the blue curve represents the smoothen behavior. Figure 6.10(d) exhibits a dip ~370 K, which is close to the onset of T_C (see Figure 6.2), peak around T_C and broad dip around T_{SRT}. It also exhibits a broad hump below 300 K, which can be considered as the precursor state of SRT, i.e., the SRT is already taking place in the form of a precursor state above actual T_{SRT} ~ 200 K. Figure 6.10(e) shows almost no change around T_C but a broad peak-like behavior around T_{SRT}. Figure 6.10(d) and Figure 6.10(e) suggest *a*-parameter dominates the paramagnetic to FM transition while *c*-parameter dominate the SRT. Further, the derivative of volume is shown in Figure 6.10(f), where the blue curve shows the smoothen behavior. The derivative of the volume shows analogous behavior to Figure 6.10(d) (derivative of *a*-parameter), i.e., dip around the onset of T_C (~370 K), peak around T_C and broad hump below 300 K, which can be considered as precursor state of SRT. It is worth mentioning here that the precursor state of SRT below 300 K (observed in Figure 6.10(d) & (e)) is reflected in the decreasing behavior of magnetization below 300 K (see the inset (i) of Figure 6.2). The peak around SRT in Figure 6.10(e) starts to develop below 300 K, which suggests that a decrease in magnetization below 300 K is due to the gradual emergence of MCA associated with the precursor state of the SRT and eventually leading to the noncollinear FM structure below T_{SRT}. Further, the *c/a* ratio (Figure 6.10(b)) exhibits slightly increasing behavior below $T_{C,}$ which suggests the increment in hexagonal distortion with decreasing temperature, which may be responsible for the increase in MCA [214]. This explains the slowly decreasing behavior of magnetization in low field *M(T)* data below T_C (see the inset (i) of Figure 6.2).

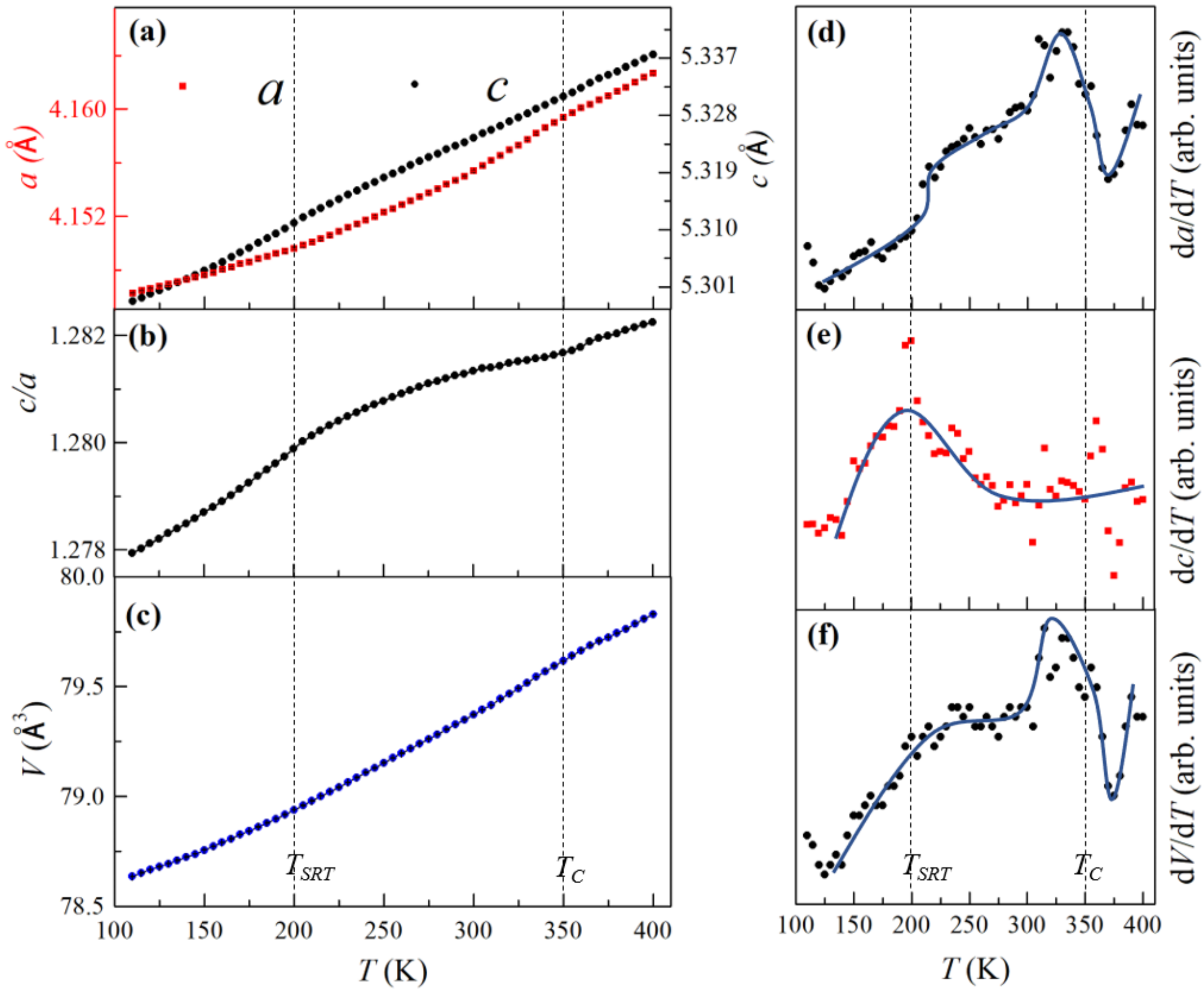

Figure 6.10: Temperature dependent behavior of (a) lattice parameters (*a* & *c*), (b) *c/a* ratio and (c) unit cell volume (*V*). The temperature derivative of *a*, *c*, and *V* are given in (d) (*da/dT*), (e) *dc/dT* and (f) *dV/dT*, respectively. The blue curve in (d), (e), and (f) represent a smoothen behavior. The transition temperatures (T_{SRT} ~ 200 K and T_C ~ 350 K) are guided by the vertical dotted line in (a)-(f).

Previous studies on NiMnGa have revealed an anomaly in the *c/a* ratio at a temperature ~250 K using synchrotron x-ray diffraction studies [214]. We believe that their anomaly in *c/a* ratio at temperature ~250 K is attributed to the precursor state as observed in our SXRPD data analysis. Their anomaly in *c/a* ratio is neither at T_{SRT} (50 K above from T_{SRT} ~ 200 K) nor at T_C [214]. In fact, they didn't succeed in capturing the change in LP or *c/a* around T_C and T_{SRT} because the diffraction data were collected in a large temperature interval of 50 K [214]. It is also important to mention that with this much of temperature interval (50 K), it is not possible to get the actual behavior of LP across SRT, which itself appears around 30 K broad (210 to 180 K) temperature window (see the red line in the inset (i) of Figure 6.2). In the present study, high-resolution SXRPD patterns are recorded in a small temperature interval of 5 K to understand the features observed in the low field magnetization (Figure 6.2). This enabled us to capture anomalies in LP, *c/a*, and *V* at both T_C and T_{SRT} temperatures for hexagonal NiMnGa. The present anomalies in LP and *V* are in agreement with those observed in a related sister compound (PtMnGa) [371], and indicate the presence of magnetoelastic coupling, which is described in the next section.

6.3.5 Magnetoelastic Coupling

The clear change in the structural parameters (LP, *c/a*, and *V*) around the magnetic transition temperatures (T_C and T_{SRT}) without any crystallographic symmetry change is an indication of magnetoelastic effects [218, 219, 394] in the FM state (below T_C) and canted spin state (below T_{SRT}). The magnetoelastic coupling deals with the coupling between magnetic and structural degrees of freedom [218, 219, 261, 394]. The magnetic phase transition around T_C and T_{SRT} may tend to perturb the lattice as NiMnGa has magnetocrystalline anisotropy, which is related to spin-lattice coupling [214, 395]. Due to a change in magnetic structure at the magnetic transitions, a perturbation in the lattice should be reflected in the structural parameters, which we have observed (see Figure 6.10) and discussed above. A qualitative description of magnetoelastic coupling by magnetoelastic coupling terms in the Landau free energy expression for the conventional second-order paramagnetic to FM phase transition is described in section 3.4.3, which suggests that the second-order paramagnetic to FM phase transition can be transformed to the firs-order, if there is sufficiently strong magnetoelastic coupling. Thus, the weakly first-order character of the paramagnetic to FM phase transition evidenced in the form of small thermal hysteresis in magnetization (see Figure 6.3(b)) and negative slope in the Arrott plots (see Figure 6.5(c)) in the hexagonal NiMnGa is essentially due to the presence of the magnetoelastic coupling. In order to investigate it experimentally, the temperature dependent volume of the hexagonal unit cell (*V*), obtained from Rietveld refinements of SXRPD data, is shown in Figure 6.11 (separately, taken from Figure 6.10(c) for the simplicity of discussion) in the temperature range of 110 K to 400 K. In order to quantify the magnetic contribution, calculated unit cell volume (V_{cal}) was obtained using Debye-Grüneisen equation, which is given below [261, 394]:

$$V_{cal} \cong V(0) + \frac{9\gamma N k_B}{B} T \left(\frac{T}{\Theta_D}\right)^3 \int_0^{\Theta_D/T} \frac{x^3}{e^x - 1}\, dx \quad .... \ (6.4)$$

Where $V(0)$, γ, k_B, B, and Θ_D are the unit cell volume at 0 K, the Grüneisen parameter, Boltzmann constant, bulk modulus, and the Debye temperature, respectively. The Θ_D is the temperature above which the collective lattice vibration vanishes. The red line in Figure 6.11 represents the V_{cal} obtained using eq. (6.4) and fitted to the experimental unit cell volume in the temperature range 360 K $\leq T \leq$ 400 K as the unit cell volume is linear within this temperature range only. The different fitted parameters are $V(0)$ = (78.66 $\pm$ 0.01) Å^3, Θ_D = 400 K and constant $9\gamma N k_B/B$ = (0.0128 $\pm$ 0.0002) Å^3/K. The difference between experimental and calculated unit cell volume (ΔV) increases with decreasing temperature below T_C (~350 K) (Figure 6.11). Ideally, the temperature dependency of experimental volume should follow the trend similar to the theoretical volume, but here it is deviating below T_C due to dominated magnetic contribution over lattice contribution. The temperature dependent bulk strain ($\Delta V/V$) in the temperature range of 350-110 K was obtained from Figure 6.11 and is plotted against the square of spontaneous magnetization

(M_S) as shown in the insets (i), (ii) and (iii) of Figure 6.11 in different temperature regions (350-300 K, 300-260 K, and 260-180 K). The M_S is obtained using high field (5 T) *M(T)* data (shown in the inset (ii) of Figure 6.2) because at such high field, the magnetization almost saturates as evidenced by *M(H)* curves (Figure 6.7(a)). The linearity of $\Delta V/V$ vs M_S^2 plots are guided by blue solid line in inset (i), (ii) and (iii) of Figure 6.11. Such linear dependence of strain ($\Delta V/V$) on M_S^2 has been termed as magnetovolume effect [261, 262]. This suggests the presence of magnetovolume effect at the FM T_C and T_{SRT} in the hexagonal NiMnGa compound. The linear dependence of strain with the square of M_S (here is the order parameter) is in agreement with expression given in eq. (3.3) of section 3.4.3, where strain (x) is proportional to the square of the order parameter (M) obtained after considering the magnetoelastic terms in Landau free energy expression (see eq. (3.2)). The presence of magnetoelastic coupling in the hexagonal NiMnGa compound manifests the weakly first-order character of the paramagnetic to FM phase transition, which is attributed to the presence of small thermal hysteresis around T_C in magnetization data (Figure 6.3(b)). Thus, due to coupling between structure and magnetism, the change in the magnetic structure during the paramagnetic to FM phase and FM to SRT transition are reflected in the unit cell volume across T_C and T_{SRT} in the hexagonal NiMnGa compound.

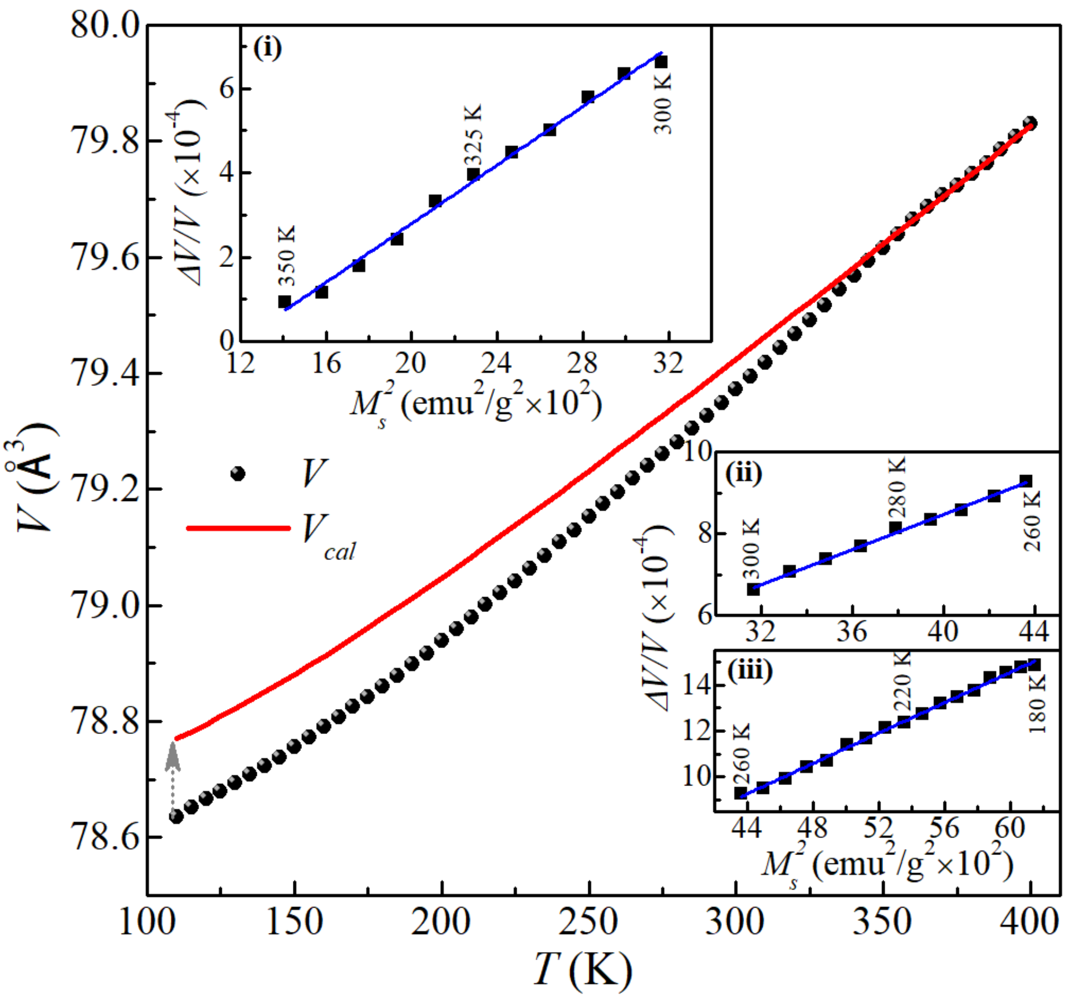

Figure 6.11: The unit cell volume (V) of hexagonal phase vs temperature plot indicated by black circles. The solid red line indicates the theoretically modeled unit cell volume (V_{cal}) using the Debye-Grüneisen equation. The grey arrow indicates the deviation between V and V_{cal}. The bulk hexagonal strain ($\Delta V/V$) vs square of spontaneous magnetization (M_S^2) plots are shown in the inset (i) for 350-300 K, inset (ii) for 300-260 K, and inset (iii) for 260-180 K, where the blue line represents the linear fitting.

6.3.6 Bond Length and Bond Angle

In order to understand the microscopic origin behind the anomalies observed in LP, *c/a* ratio, and unit cell volume around T_C and T_{SRT} (Figure 6.10), we investigated the behavior of bond length and bond angle around these magnetic transitions. The temperature dependency of bond lengths and their derivatives are shown in Figure 6.12(a)-(f), while temperature dependency of bond angles is shown in Figure 6.13(a), where vertical dashed lines guide the T_C and T_{SRT} temperatures. The atoms considered in the bond lengths and bond angles are indicated in Figure 6.13(b). A clear anomaly was observed around T_C in the Ni-Ga and Ni-Mn (or Ga-Mn) bond lengths as revealed by a peak-like behavior around T_C in their derivatives (see Figure 6.12(d) & (f)). The closest Mn-Mn distance, which is equivalent to half of the *c*-parameter (i.e., *c*/2), is shown in Figure 6.12(b). Around T_C, the anomaly in derivative of *c*-parameter (or *c*/2) (see Figure 6.10(e) or Figure 6.12(e)), i.e., Mn-Mn bond distance is relatively weak in comparison to Ni or Ga mediated bond distances (i.e., Ni-Ga, Ni-Mn) (see Figure 6.12(d) & (f)). This suggests the paramagnetic to FM phase transition T_C ~ 350 K is mainly governed by Ni-Ga and Ni-Mn mediated exchange interactions. Interestingly, around T_{SRT} ~ 200 K anomaly in closest Mn-Mn bond distance is much more pronounced (as evident by a peak in the derivative of Mn-Mn bond distance in Figure 6.12(e)), on the other hand the anomalies observed in the derivative of Ni-Ga and Ni-Mn are relatively weaker (Figure 6.12(d) & (f)).

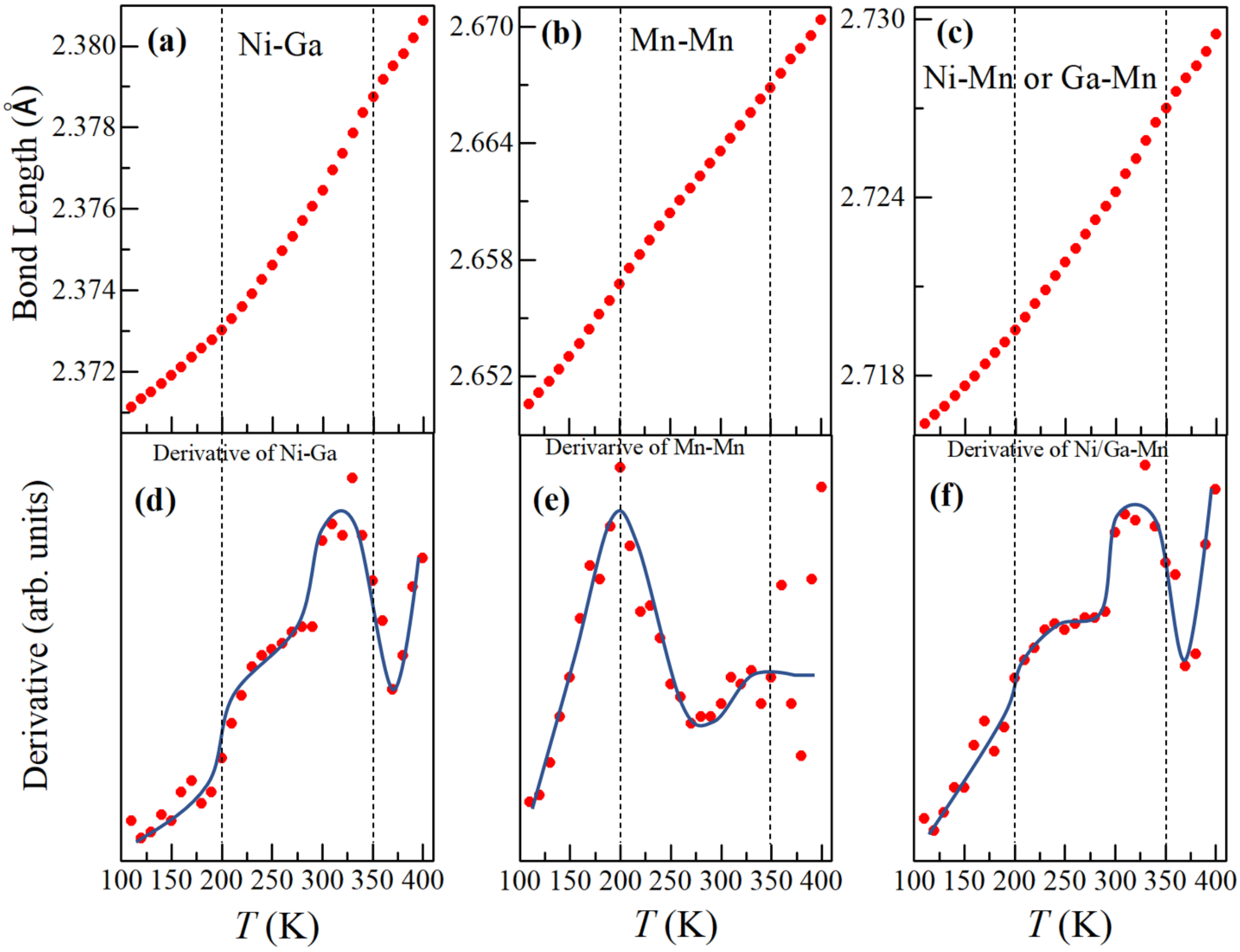

Figure 6.12: The bond length corresponding to (a) Ni-Ga, (b) Mn-Mn, and (c) Ni-Mn or Ga-Mn pairs. The temperature derivative of (d) Ni-Ga, (e) Mn-Mn, and (f) Ni-Mn or Ga-Mn, pairs. The blue curve in (d)-(f) represents a smoothen behavior. The transition temperatures $T_C \sim 350$ K and $T_{SRT} \sim 200$ K are guided by the vertical dotted line.

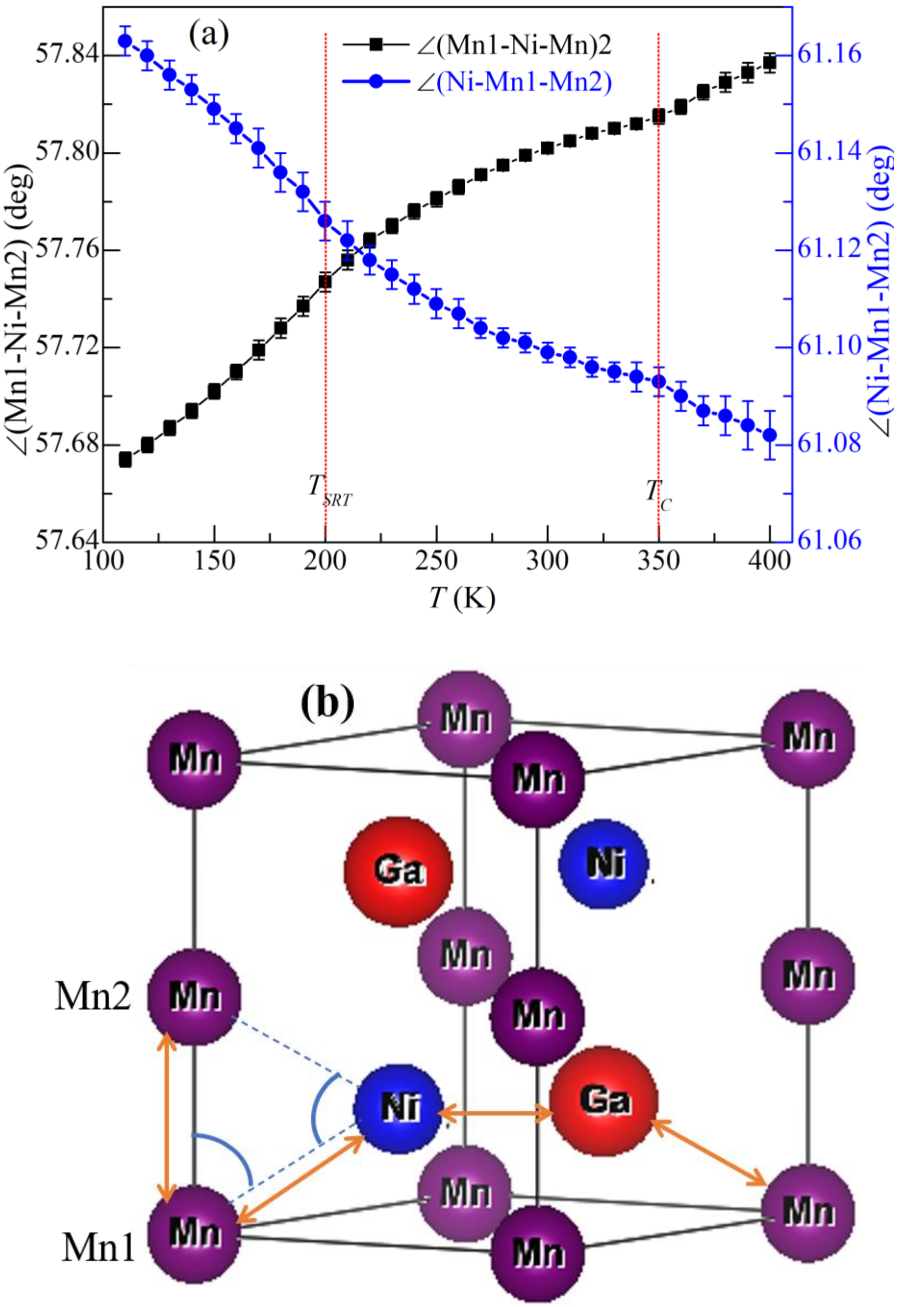

Figure 6.13: (a) Temperature dependency of bond angle corresponding to Mn1-Ni-Mn2 and Ni-Mn1-Mn2. The slope change around T_C ~ 350 K and T_{SRT} ~ 200 K are guided by the vertical dotted line. (b) The unit cell of NiMnGa, where the position of atoms involved for bond lengths (shown in Figure 6.12) and bond angles (shown in Figure 6.13(a)) are indicated (by arrows and angle) for the sake of visualization.

This suggests that the closest Mn-Mn mediated exchange interactions mainly govern the SRT. We believe that the closest Mn-Mn distance adjusts themselves to facilitate the transition from FM state to spin canted state at T_{SRT}. This supports the earlier theoretical study, which predicts that the shortest Mn-Mn distance governs the magnetism in the hexagonal NiMnGa [215]. The hump-like region below 300 K in Figure 6.12(d) & (f) is related to the precursor state of SRT as discussed above in the context of Figure 6.10(d) & (f). Further, the bond angle of Ni situated nearest to the closest Mn1-Mn2 distance is shown in Figure 6.13(a), which shows that bond angle Mn1-Ni-Mn2 decreases while bond angle Ni-Mn1-Mn2 are increasing with lowering the temperatures. As expected, clear anomalies appear around T_C and T_{SRT} temperatures as guided by vertical dash lines in Figure 6.13(a). Looking closely around T_C, the angle Mn1-Ni-Mn2 increases while Ni-Mn1-Mn2 decreases just below T_C. The anomalies around T_C and T_{SRT} present in bond lengths and bond angles are responsible for the anomalies in the structural parameters (see Figure 6.10(a)) and further attribute magnetoelastic coupling in the hexagonal NiMnGa.

6.3.7 Thermal Expansion Behavior

The thermal expansion is defined by the ratio of change in dimension (ΔL) to the original dimension (L_0) of the specimen with a change in temperature. The thermal expansion was calculated using LP and V, obtained from temperature dependent Rietveld refinements of the SXRPD data, and shown in Figure 6.14(a)-(c). Although the obtained thermal expansions have a slight fluctuation with temperature, a clear change is observable around both magnetic transitions (T_C and T_{SRT}). With decreasing temperature from 400 K, the thermal expansion corresponding to a-parameter ($\Delta a/a$) starts to increase around 370 K, which is the close to the onset of ferromagnetic T_C, and then peak-like behavior is observed around $T_C \sim 350$ K (Figure 6.14(a)). Apart from peak behavior around T_C, a nearly temperature independent (or flat) region appears in the temperature range of 275-225 K (see Figure 6.14(a)). This temperature independent region is related to the precursor state of SRT as discussed above in the context of Figure 6.10(d) & (f) and Figure 6.12(d) & (f). The thermal expansion corresponds to c-parameter ($\Delta c/c$) exhibit usual decreasing behavior around $T_{C,}$ but a sharp peak appears around T_{SRT} (Figure 6.14(b)). This sharp peak around T_{SRT} suggests that the SRT is mainly governed by c-parameter as observed in the derivate of c-parameter (Figure 6.10(e)). The thermal expansion corresponding to V (i.e., $\Delta V/V$) is shown in Figure 6.14(c), which reveals a similar trend like a-parameter. This behavior in $\Delta V/V$ is expected because the volume of hexagonal unit cell has the dominant contribution of a-parameter ($V = \frac{\sqrt{3}}{2} * a^2 * c$). The appearance of peak and temperature independent regions in the thermal expansion is the signature of the anomalous thermal expansion (ATE) and zero thermal expansion (ZTE), respectively. On the other hand, an ordinary decrease of thermal expansion with the decrease in temperature manifests the positive thermal expansion behavior (PTE) [363]. The regions of ATE, ZTE, and PTE are indicated with the help of red arrows and vertical lines in Figure 6.14(a) to (c). Here, the appearance of ZTE manifests the Invar effect as reported in the group-I compounds [200]. The linear thermal expansion coefficient (TEC; α) can be defined as the ratio of change in dimension (ΔL) to original dimension (L_0) of the specimen with the change in temperature (ΔT), i.e., $\alpha = \frac{\Delta L}{L_0 * \Delta T}$. We calculated TEC using LP (a & c) and V, and indicated them by α_a, α_c, and α_V, respectively. The as $\alpha_a \sim 17\ \mu K^{-1}$ and $\alpha_V \sim 58\ \mu K^{-1}$ were obtained in the ATE regions around T_C as indicated by blue arrows in Figure 6.14(a) and (c). The $\alpha_c \sim 26\ \mu K^{-1}$ was obtained around T_{SRT}. The thermal expansion has been reported for the group-I compounds like MnCoGe [363] and MnNiGe [200] using a dilatometer, which provides the macroscopic and average/isotropic change in dimension of the specimen with a change in temperature.

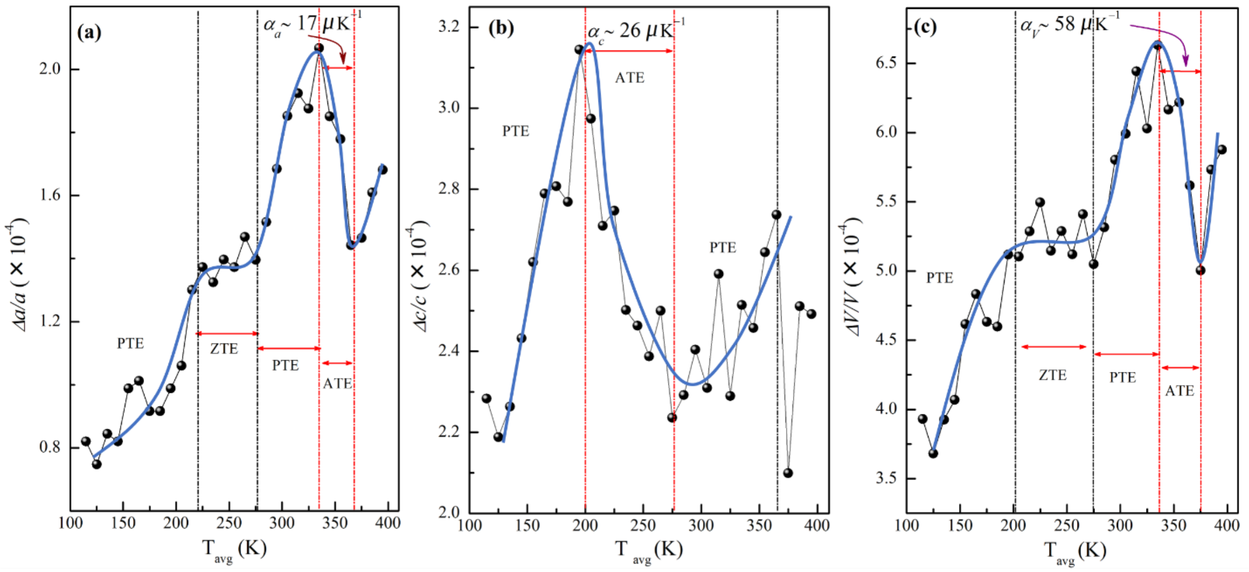

Figure 6.14: Thermal expansion vs temperature plot corresponding to (a) *a*-parameter (*Δa/a*), (b) *c*-parameter (*Δc/c*) and (c) unit cell volume (*ΔV/V*). The blue curve represents smoothened behavior. The anomalous, positive, and zero thermal expansion regions are guided by dashed lines and red arrows. The ZTE, ATE, and PTE represent the zero-thermal expansion, anomalous thermal expansion, and positive thermal expansion, respectively. The thermal expansion coefficient corresponding to *a*-parameter, *c*-parameter, and unit cell volume is indicated by α_a, α_c and α_V, respectively.

The α of the present study appears in 10^{-6} scale, which is in agreement with the TEC value reported for the group-I compounds like MnCoGe [363] and MnNiGe [200] for e.g., $\alpha \sim 71.2$ μK^{-1} in the temperature range of 145 K has been reported for $MnCoGe_{0.99}$. In our case, $\alpha_V \sim 58$ μK in the temperature range of 40 K is obtained for NiMnGa. Further, we have calculated the TEC using LP and *V*, obtained from SXRPD data analysis, which provides atomic-level information, i.e., it can be considered as microscopic TEC. The signature of ATE associated with in-plane lattice parameter (*a*-parameter) and unit cell volume is observed across T_C while ATE is observed across T_{SRT} for *c*-parameter. This suggests the anisotropic thermal expansion behavior in NiMnGa as observed in the related (group-I) compound [197].

6.3.8 Structural Investigation Under Hydrostatic Pressure

It has been proposed that the stability of skyrmion textures is very sensitive to external uniaxial stress or pressure, which can manipulate these spin textures through spin-lattice coupling [221-223]. Since NiMnGa host biskyrmions [187] and possess spin-lattice coupling as described in section 6.3.5, a detailed study of the crystal structure of NiMnGa with external hydrostatic pressure is presented here to understand the pressure-tuning of biskyrmions in NiMnGa. The Rietveld refinement using the SXRPD data of NiMnGa at ambient condition is shown in Figure 6.15, which shows an excellent fit between observed and calculated profiles by accounting for all the Bragg peaks for $P6_3/mmc$. The refinement confirms the monophasic nature of the powder in the hexagonal $P6_3/mmc$ space group of NiMnGa. The refined lattice parameters were found to be $a = b = 4.1574(1)$ Å and $c = 5.3261(1)$ Å, which are in close agreement with those obtained from SXRPD at 300 K (discussed in section 6.3.4). However, the intensity of (110) Bragg reflection should be higher than (102) as observed in the SXRPD pattern (see inset of Figure 6.8(a)) and also in the theoretically calculated diffraction pattern, a reverse situation in the SXRPD data at the ambient condition (see Figure 6.15) is certainly due to texturing effect.

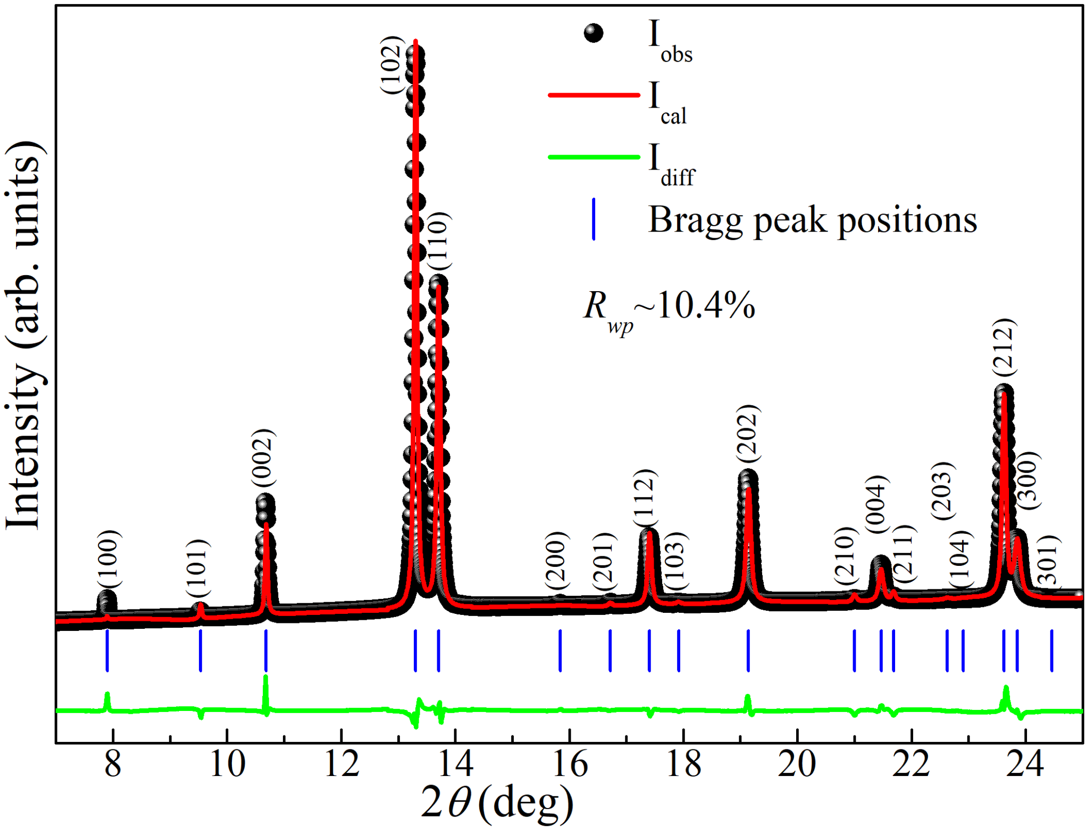

Figure 6.15: The observed (black spheres), calculated (continuous red line), and difference profiles (bottom green line) obtained after Rietveld refinement using synchrotron x-ray powder diffraction pattern at the ambient condition in the $P6_3/mmc$ space group of NiMnGa. The vertical tick marks above the difference profile represent the Bragg peak positions. The "R_{wp}" represents the weighted agreement factor of the fitting. The miller indices are given above each reflection.

The SXRPD patterns under high-pressure (0-14 GPa) are shown in Figure 6.16(a), whose enlarged view around the most intense Bragg peak region is depicted in Figure 6.16(b). In Figure 6.16, the absence of any splitting or appearance of additional Bragg peaks with pressure manifests that the hexagonal symmetry remains preserved. This indicates the absence of any structure phase transition in NiMnGa with pressure up to 14 GPa, the maximum pressure up to which data has been collected. Further, the systematic shifting of the Bragg peaks to the higher 2θ side with pressure suggests the compression of lattice parameters or interplanar spacings (see Figure 6.16).

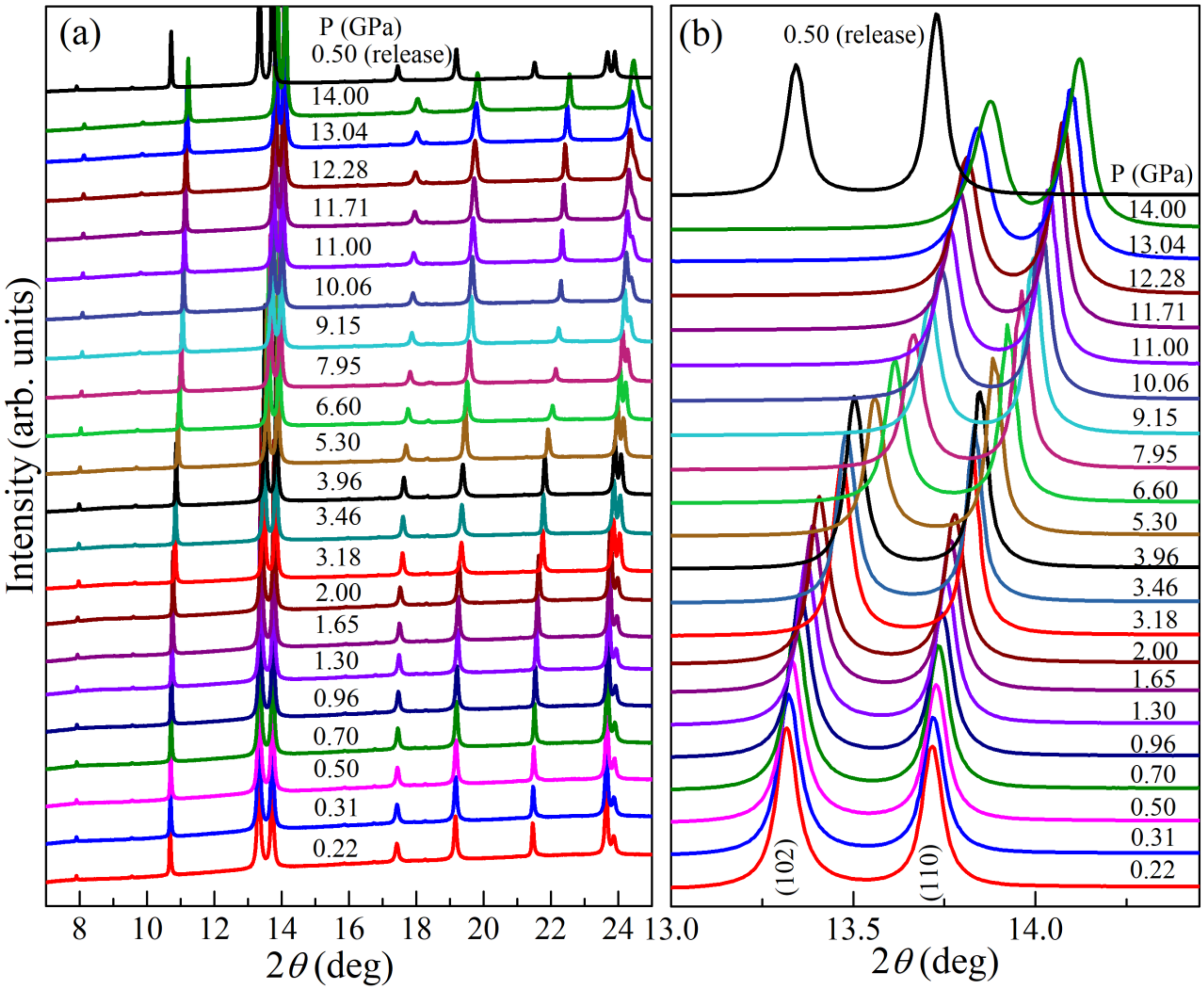

Figure 6.16: (a) The synchrotron x-ray powder diffraction pattern collected at various pressure (indicated) up to 14 GPa. (b) The enlarged view around the most intense Bragg peak region. The miller indices of both major peaks are given in the bottom-most in (b). The "P (GPa)" represents the pressure in the GPa unit. The topmost pattern labeled by "0.50 (release)" was collected during releasing the pressure with effective pressure of 0.50 GPa.

At P ≥ 3.96 GPa, the intensity of (110) reflection became higher than (102) reflection (i.e., intensity switching), which suggests the texturing effect observed at low pressure is suppressed at higher pressure (see Figure 6.16(b)). All of these behaviors in the data were found to be reversible with pressure, as demonstrated by comparison of the bottom SXRPD pattern, which was collected at 0.22 GPa during pressure application, and the top SXRPD pattern, which was collected at 0.5 GPa during pressure release. This indicates reversibility of structure with the pressure effects, i.e., after releasing the pressure, complete recovery of the structure to the ambient conditions. This reversibility behavior with pressure in NiMnGa is in marked contrast to other skyrmion host Cu_2OSeO_3, wherein the irreversibility behavior with pressure has been observed [385]. In Cu_2OSeO_3, cubic to monoclinic phase transition at 7 GPa and then monoclinic to triclinic phase transition at 11 GPa has been reported [385]. But after releasing the pressure, a new monoclinic phase was observed instead of the cubic phase, i.e., irreversibility of phase transition with pressure in Cu_2OSeO_3 [385]. The reversibility behavior of NiMnGa makes this alloy system ideal for pressure-tuning of skyrmion textures.

The lattice parameter was obtained from the Rietveld refinement using high-pressure SXRPD data with $P6_3/mmc$ space group. The evolution of lattice parameters (a and c) with pressure are shown in Figure 6.17(a) and (b). However, the behavior of lattice parameters at low pressure shows linear compression as indicated by a linear fit to the observed lattice parameter, a clear departure from the linearity observed above 4 GPa in the form of deviation between extrapolated linear fit and the data in Figure 6.17(a) and (b). The slope of the linear fit to in-plane (a) and out of the plane (c) lattice parameter was found to be $da/dP \approx -0.01126$ Å GPa^{-1} and $dc/dP \approx -0.02306$ Å GPa^{-1}, respectively (see Figure 6.17(a) and (b)). This means a higher compression rate for the out of plane c-axis in comparison to the in-plane a-axis with pressure, i.e., presence of anisotropic compression behavior in the NiMnGa as reported in the other hexagonal system [387]. To visualize the present anisotropic compression, a unit cell of NiMnGa is depicted in Figure 6.17(c), wherein the higher compression rate in the out of plane lattice parameters in comparison to lower compression rate for in-plane lattice parameters is indicated by lower length of spring connected with arrows along *c*-axis than the in-plane, respectively.

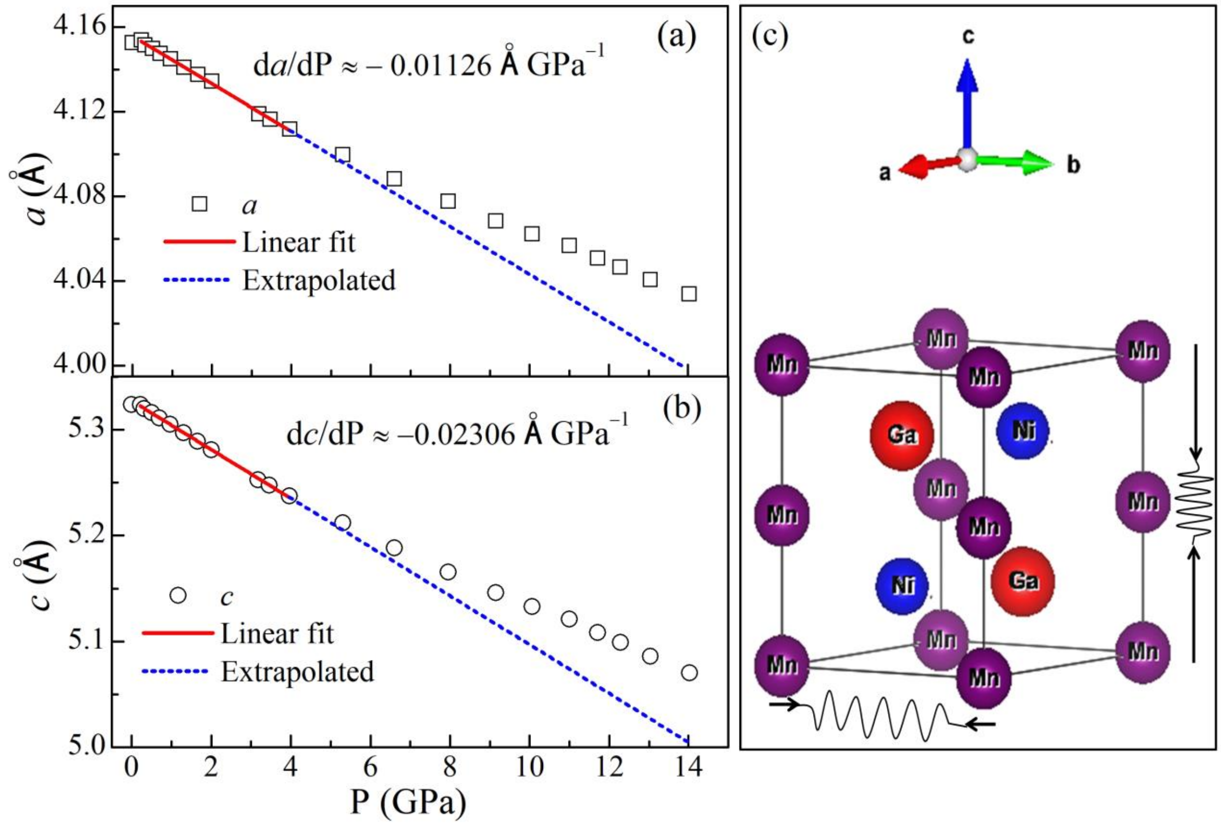

Figure 6.17: Pressure-dependence of (a) in-plane and (b) out of plane lattice parameters of NiMnGa. The red line and dotted blue line in (a) and (b) represent the linear compression and extrapolated region of linear compression behavior, respectively. The "d*a*/dP" and "d*c*/dP" indicate the linear compression rate in *a* and *c*-parameter in (a) and (b), respectively. The error in lattice parameters is smaller than the symbol size. (c) The unit cell of NiMnGa, wherein different lengths of springs connected with arrows indicate the different compression rates in the in-plane and out-of-plane lattice parameters.

In addition to the lattice parameters, the deviation from the systematic linearity with pressure above 4 GPa is also observed in unit cell volume (*V*) and *c/a* ratio as depicted in Figure 6.18 and in the inset of Figure 6.18, respectively. The decreasing behavior of the *c/a* ratio with pressure further manifests that the *c*-axis is more compressible than the *a*-axis (see inset of Figure 6.18). This behavior is usually expected for anisotropic crystals due to the weak van der Waals interlayer forces along the *c*-direction [387].

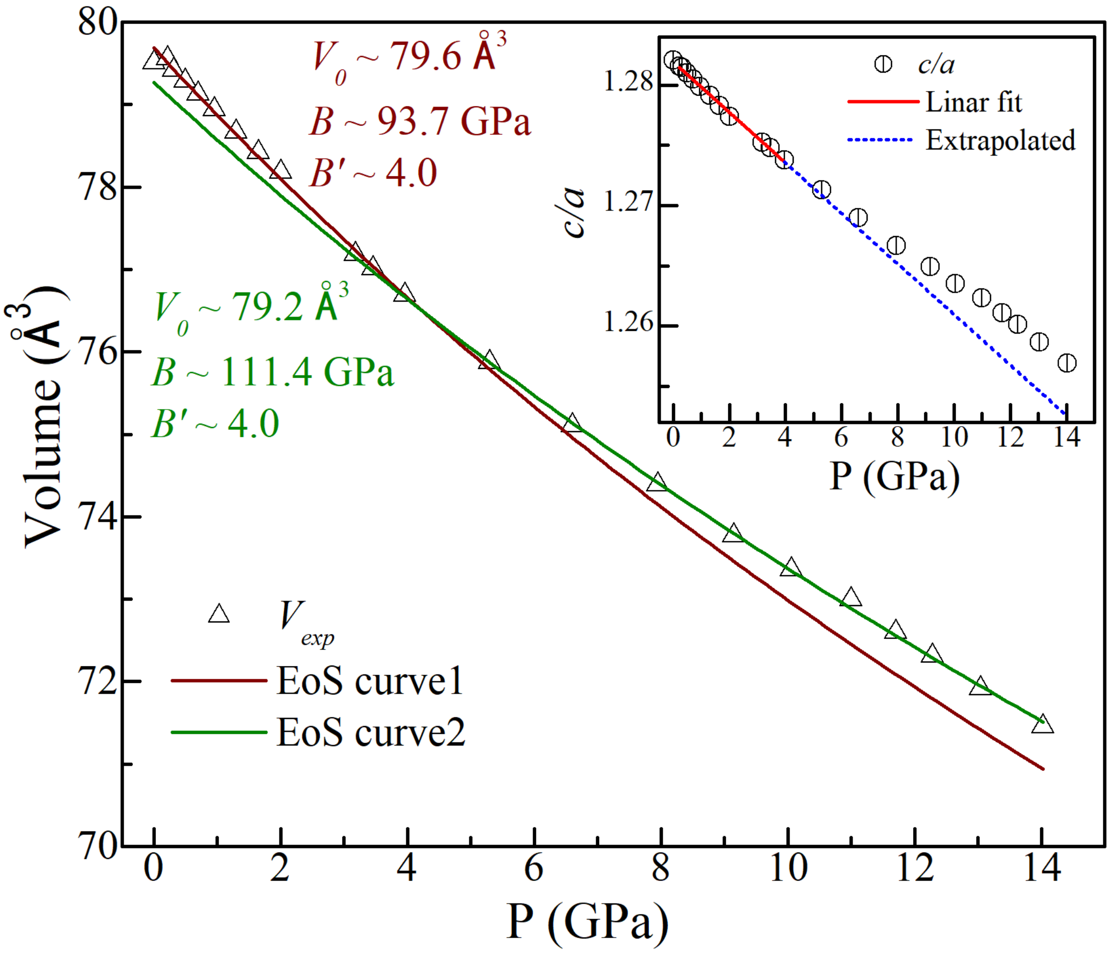

Figure 6.18: Pressure-dependence of unit cell volume (*V*). Solid lines indicate the results of a second-order Birch–Murnagan equation-of-state (EoS) fit to the data. "EoS1" and "EoS2" represent the fitting considering the data upto 4 GPa and above 4 GPa, respectively. The V_0, *B*, and *B′* are the parameters obtained from the fit. Pressure dependence of *c/a* ratio is depicted in the inset, wherein the red line and dotted blue line represent the linear fit and extrapolation of the linear fit, respectively. The error in *V* and *c/a* are smaller than the symbol size.

The significant deviation in the structural parameters (*a*, *c*, *c/a*, and *V*) above 4 GPa from the linearity without any change in symmetry is the indication of isostructural phase transition [387, 388, 396]. In order to investigate it, a second-order Birch–Murnagan equation-of-state [397, 398] (2nd O B-M EoS) was employed to model the evolution of volume with pressure (P-*V*) using the EoSFit7-GUI software [399]. The standard B-M EoS is given below:

$$P\ (V) = \frac{3B}{2}\left[\left(\frac{V_0}{V}\right)^{7/3} - \left(\frac{V_0}{V}\right)^{5/3}\right] \times \left\{1 + \frac{3}{4}(B' - 4)\left[\left(\frac{V_0}{V}\right)^{2/3} - 1\right]\right\} \ldots \ (6.5)$$

In eq. (6.5), V, V_0, B, and B' are volume, reference volume, bulk modulus, and pressure derivative of bulk modulus, respectively [396]. To get the second-order B-M EoS, the value of B' is considered as 4 in eq. (6.5). Since considering the whole P-*V* region together did not yield a satisfactory fit, two separate regions of the P-*V* plot were considered for the fitting using two independent 2nd O B-M EoS. The first region was considered at the lower pressure side (up to GPa), while the second is at the higher-pressure side (above 4 GPa). The result of the fitting is shown in Figure 6.18, which yield different bulk modulus (*B*) for different region. The value of *B* was found to be increased from ~93.7 GPa to ~111.4 GPa from low to high-pressure regions. In skyrmion host Cu_2OSeO_3, cubic to monoclinic phase transition has been observed at 7 GPa with *B* increased from 74.8 to 161.1 GPa [385]. Compared to this, a relatively smaller change in *B* (~93.7 to ~111.4 GPa) of NiMnGa manifests the pressure-induced isostructural phase transition above 4 GPa and suggests that the high-pressure phase has lesser compressibility than the low-pressure phase in NiMnGa as reported in other systems (like PdPS[42]). The presence of pressure-induced isostructural phase transition is of fundamental importance and opens a new pathway for future investigation of pressure-tuning of skyrmion textures in the centrosymmetric NiMnGa and related system.

The maximum density of biskyrmions has been reported at T_{SRT} ~ 200 K [187], where AFM components increase significantly due to spin canting [214]. Further, the application of pressure at room temperature compresses the lattice and result into the reduced Mn-Mn interatomic distances, which results in the modification of magnetic interactions. Therefore, a natural question arises: can SRT be induced at room temperature with pressure? This will help stabilize the maximum density of biskyrmions at room temperature in NiMnGa and lead to low power consumption in the spintronic devices [214]. In order to investigate that, the temperature dependent and pressure dependent lattice parameters (LP) obtained after Rietveld refinements are compared in Table 6.2, which reveals that LP at 200 K (~T_{SRT}) are close to the LP at 0.7 GPa. This suggests that T_{SRT} or maximum density of biskyrmions can be stabilized at room temperature by using P ~ 0.7 GPa.

Table 6.2: Comparison of lattice parameters (*a* and *c*) with temperature and pressure of hexagonal NiMnGa.

Temperature	**Lattice Parameters (Å)**	**Pressure**	**Lattice Parameters (Å)**
300 K	*a* = 4.15538(5) *c* = 5.3245(1)	0 GPa	*a* = 4.1552(2) *c* = 5.3246(3)
200 K (~T_{SRT})	*a* = 4.1496(4) *c* = 5.3110(2)	0.7 GPa	*a* = 4.1485(2) *c* = 5.3118(3)
110 K	*a* = 4.14626(6) *c* = 5.2986(1)	0.96 GPa	*a* = 4.1462(2) *c* = 5.3064(3)

6.4 Conclusions

To summarize, we presented the magnetic and crystal structure evolution of the hexagonal NiMnGa using magnetization and SXRPD data. The low field magnetization revealed deviation from standard order parameter and exhibits an anomalous decrease below FM T_C, suggesting the gradual emergence of MCA eventually leading to the noncollinear FM structure below T_{SRT}. The presence of small thermal hysteresis in the magnetization and negative slope in the Arrott plots across FM T_C confirmed the weakly first-order character of paramagnetic to FM phase transition. The structural parameters (*a*, *c*, *V*, *c/a*, bond lengths, and bond angles) revealed anomalies around T_C as well as T_{SRT} and indicated the precursor effect of SRT. The magnetoelastic contribution to the unit cell volume is shown to scale with the square of spontaneous magnetization in the FM as well as SRT phase, confirming the presence of magnetovolume effect. The linear TEC, obtained from the temperature dependent of *a*, *c* and *V* revealed anomalous, positive, and nearly zero thermal expansion behaviors in different temperature regions. More significantly, our results revealed that the dominant role of Ni-Ga and Ni-Mn mediated exchange interactions in the paramagnetic to FM transition, while Mn-Mn exchange interaction dominates in the FM to SRT of NiMnGa. We believe that our magnetoelastic coupling results may provide insight into understanding the extreme sensitivity of the skyrmionic textures to external stresses. In addition, we have also shown the pressure-induced isostructural phase transition in the hexagonal NiMnGa using high-pressure SXRPD analysis. Our SXRPD data revealed anisotropic compression behavior with pressure with different compression rates of the *a*-axis in the basal plane and the *c*-axis in the prismatic plane. However, the hexagonal symmetry remains unchanged for pressure up to 14 GPa. Modeling of unit cell volume with pressure using a second-order Birch–Murnagan equation of state revealed that the data to fall into two distinct curves for those above and below 4

GPa. The present pressure dependent SXRPD study contributes to the understanding of crystal structure with external pressure tuning in the biskyrmion host NiMnGa wherein the spin textures can be manipulated by pressure due to their magnetoelastic nature.